

## ABSTRACT

MILLER, MATTHEW ALLEN. Satellite Observations of Low Marine Clouds. (Under the direction of Sandra E. Yuter.)

This dissertation uses satellite passive microwave data sets to address two subtypes of low marine clouds: stratocumulus clouds that are atypically-thick ( $> 2$  km) and canonical stratocumulus clouds that contain discrete drizzle cells.

Understanding the characteristics and behavior of low marine clouds is of critical importance for climate research and prediction. Low clouds, as a group, cover a large part of the world's oceans and have a strong effect on the radiation budget and global temperature regulation which has important climate implications. Low marine clouds reflect a large amount of short-wave solar radiation back into space before it can heat the earth's surface. As a result, low marine clouds have a net cooling effect and they are considered to act as a mitigating force against global warming. Currently, low clouds are not well represented in numerical climate models. This known deficiency calls into question the accuracy of the radiative balance in climate models which directly affects the accuracy of predictions of temperature and the impacts of climate change. In order to improve climate predictions, climate models will need to better represent the physical processes behind low marine clouds and their distributions in order to improve predictions of current and future climate. This study addresses deficiencies in the understanding of low marine clouds that has the potential to improve how subsequent climate models handle low marine clouds.

Atypically-thick low marine clouds are low stratiform marine clouds with a thickness greater than 2 km that occur in continuous sheets, usually tens to hundreds of kilometers across, and do not produce rain greater than  $0.4 \text{ mm hr}^{-1}$  (i.e. the passive microwave sensor detectable threshold). This subset of cloud has not been previously classified. Two potential formation mechanisms are inferred based on the environmental background data: steam fog/cold air outbreak genesis and advection fog/warm front genesis. Mixing

processes deepen the cloud layer and disperse the vertically-integrated liquid water content over a longer path, reducing the volumetric liquid water content. Atypically-thick low marine clouds occur most commonly in the winter hemisphere on the lee side of continents at latitudes between  $15^{\circ}$  and  $60^{\circ}$  from the equator. For localized regions, upwards of 30% of monthly and 10% of annual passive microwave satellite observations can have an atypically-thick low marine cloud radiative signature. In ocean regions near continents, these clouds appear to be associated with cold air outbreaks over warm sea surface temperatures (steam fog), but they can also occur over open ocean associated with extratropical cyclones (advection fog). Atypically-thick low marine clouds occur in areas with different levels of aerosol pollution, ranging from very polluted areas to areas with very low aerosol amounts.

Drizzle has been identified as playing a key role in the evolution of marine stratocumulus and the transitions between closed and open cellular states. Current satellite methods capable of monitoring drizzle are either lacking in resolution or diurnal coverage. Using high-frequency passive microwave observations from the AMSR-E sensor to detect drizzle in marine stratocumulus allows for consistent observations at resolutions sufficient for resolving individual heavy drizzle cells. Use of the AMSR-E 89 GHz  $6 \text{ km} \times 4 \text{ km}$  brightness temperatures reduces beam-filling errors compared to current AMSR-E liquid water path products. The drizzle proxy product based on AMSR-E 89 GHz information represents a new approach using downward-looking passive microwave data that provides information on the frequency of occurrence and spatial characteristics of drizzle with the aim of better understanding the role of drizzle in the evolution of marine stratocumulus.

Satellite Observations of Low Marine Clouds

by  
Matthew Allen Miller

A dissertation submitted to the Graduate Faculty of  
North Carolina State University  
in partial fulfillment of the  
requirements for the Degree of  
Doctor of Philosophy

Marine, Earth, and Atmospheric Sciences

Raleigh, North Carolina

2010

APPROVED BY:

---

Anantha Aiyyer

---

Scott Braun

---

Sankar Arumugam

---

Sandra Yuter  
Chair of Advisory Committee

## **ACKNOWLEDGEMENTS**

I would like to thank Dr. Sandra E. Yuter for her continuous support, assistance, guidance, patience, and faith. I would like to thank my various lab mates for being there to bounce ideas off of and for providing a pleasant distraction when work became too wearisome. I would like to thank Dr. Anantha Aiyyer, Dr. Sankar Arumugam, and Dr. Scott Braun for their time and effort spent serving on my advisory committee. I would like to my family for their unwavering support and encouragement. Last, but far from least, I would like to thank my wife, Christina. Her infinite tolerance and understanding enabled her to accept the fact that I work best during hours when she would rather have me home; hours when normal people sleep.

# TABLE OF CONTENTS

<b>List of Figures.....</b>	<b>viii</b>
<b>List of Tables .....</b>	<b>ix</b>
<b>Chapter I Introduction.....</b>	<b>1</b>
<b>Chapter II Satellite Observations of Atypically-Thick Low Marine Clouds.....</b>	<b>6</b>
2.1 Introduction.....	6
2.2 Data and Methodology.....	9
2.2.1 TRMM Microwave Imager.....	9
2.2.2 AMSR-E .....	11
2.2.3 Model Reanalysis.....	12
2.2.4 CloudSat.....	12
2.2.5 Auxiliary Data.....	13
2.2.6 Identifying Atypically-Thick Low Marine Clouds .....	13
2.2.7 Using Search Algorithm with AMSR-E to Find Relevant CloudSat Data.....	16
2.3 Examples of Atypically-Thick Low Marine Clouds.....	17
2.3.1 Advection Fog Genesis .....	17

2.3.2 Steam Fog Genesis.....	19
2.3.3 Steam Fog over East China Sea.....	22
2.3.4 Moisture Profiles.....	25
2.4 Global Distribution of Atypically-Thick Low Marine Clouds.....	28
2.4.1 Annual Patterns.....	28
2.4.2 Seasonal Patterns.....	30
2.4.3 Diurnal Patterns.....	30
2.5 Conclusions.....	31
<b>Chapter III The Feasibility of Satellite 89 GHz Passive Microwave Measurements for the Detection and Characterization of Drizzling Marine Stratocumulus.....</b>	<b>56</b>
3.1 Introduction.....	56
3.2 Methodology.....	59
3.2.1 Background Emissitivity.....	60
3.2.2 Identification of Drizzle Cells.....	60
3.3 Stratocumulus Detection Examples.....	63
3.3.1 Southeast Pacific.....	63

3.3.2 Southeast Atlantic .....	65
3.3.3 Northeast Pacific .....	65
3.4 Conclusions .....	66
<b>Chapter IV Future Work.....</b>	<b>78</b>
4.1 Atypically Thick Low Marine Clouds .....	78
4.1.1 Quantifying Passive Microwave Precipitation Bias .....	78
4.1.2 MODIS Cloud Properties Analysis.....	79
4.1.3 Systematic CloudSat Thickness Assessment .....	80
4.1.4 Field and Modeling Studies .....	81
4.2 Using 89 GHz Drizzle Detection for Climate Study .....	82
<b>References.....</b>	<b>84</b>

## LIST OF TABLES

Table 2.1	Comparison and TRMM versus AMSR-E Characteristics and Features...35
Table 2.2	Atypically-Thick Low Marine Clouds Training Cases.....36
Table 2.3	Summary of Atypically-Thick Low Marine Cloud Filtering Criteria .....37
Table 2.4	Autoconversion threshold criteria for example cases .....38

## LIST OF FIGURES

Figure 2.1	Average percent low cloud amount based on monthly ISCCP-D2 visible and infrared satellite data from July 1983 through June 2008.....	39
Figure 2.2	Matrix of brightness temperature distributions for 60,000 atypically-thick low marine cloud pixels randomly sampled across the TMI domain for 2004. The histograms and scatter density plots show the brightness temperature distributions of atypically-thick low marine cloud for each vertically polarized TMI channel. ....	40
Figure 2.3	Atypically-thick low marine cloud in the eastern Gulf of Mexico on 5 March 2002. The black area is atypically-thick low marine cloud as flagged by the search algorithm. The blue areas denote cloud that was excluded by the contiguous area filter. The red boundary represents the edges of the atypically-thick low marine cloud and is overlaid over the 10 GHz, 19 GHz, 21 GHz, 37 GHz, and 85 GHz vertically-polarized TMI brightness temperatures. ....	41
Figure 2.4	Algorithm-identified atypically-thick low marine cloud (red) overlaid TMI near-surface rain rate for TRMM orbit 44633 on 14 September 2005 in the vicinity of Tropical Depression Jove in the eastern Pacific Ocean. The red atypically-thick low marine cloud	

area is removed since the contiguous areas are less than  $50 0.1^\circ \times 0.1^\circ$  pixels. ....42

Figure 2.5 Atypically-thick low marine cloud (a) and CloudSat reflectivity profile (b) data from 29 August 2008. The green line in panel a) denotes the corresponding CloudSat ground path. The red box in both panels a) and b) highlights the area indentified as atypically-thick low marine clouds by the search algorithm. Panel c) is the Aqua MODIS band-31 IR blackbody-equivalent brightness temperatures. Panel d) is the 925 hPa winds from the NCEP/DOE model reanalysis for 18 UTC 29 August 2008. Panel e) is the Remote Sensing Systems Passive Microwave plus Infrared Optimally Interpolated version 1 Sea Surface Temperature for 29 August 2008. Panel f) is the 2 m temperature from the NCEP/DOE model reanalysis for 18 UTC 29 August 2008. ....43

Figure 2.6 Schematic of the processes inferred in the transition from advection fog into atypically-thick low marine cloud. ....44

Figure 2.7 Atypically-thick low marine cloud (a) and CloudSat reflectivity profile (b) data from 3 January 2008. The green line in panel a) denotes the corresponding CloudSat ground path. The red box in both panels a) and b) highlights the corresponding feature of interest in each panel. Panel c) is the Aqua MODIS band-31 IR

blackbody-equivalent brightness temperatures. Panel d) is the 925 hPa winds from the NCEP/DOE model reanalysis for 18 UTC 3 January 2008. Panel e) is the Remote Sensing Systems Passive Microwave plus Infrared Optimally Interpolated version 1 Sea Surface Temperature for 3 January 2008. White denotes land. Panel f) is the 2 m temperature from the NCEP/DOE model reanalysis for 18 UTC 3 January 2008. Panel g) is the Remote Sensing Systems TMI 0.25° cloud water path data for 3 January 2008. Black areas denote either land or missing data. ....45

Figure 2.8 Schematic of the processes inferred in the transition from steam fog into atypically-thick low marine cloud. ....46

Figure 2.9 Atypically-thick low marine cloud off the Taiwan coast on 1 Feb. 2000. (a) TMI surface precipitation retrieval. (b) PR near surface precipitation. (c) Coastal S-band radar composite. Ring denotes maximum range. (d) 14 km TMI cloud ice above observed cloud top level. (e) Atypically-thick low marine cloud (black). Dark grey denotes land and light grey denotes TMI swath area. (f) TRMM infrared blackbody-equivalent brightness temperatures. ....47

Figure 2.10 Additional data sets corresponding to 1 Feb. 2000 case shown in Fig. 2.9. Panel a) is the 925 hPa winds from the NCEP/DOE model reanalysis for 12 UTC 1 February 2000. Panel b) is the Remote

Sensing Systems TMI Optimally Interpolated version 1 Sea Surface Temperature for 1 February 2000. The white area denotes land. Panel c) is the 2 m temperature from the NCEP/DOE model reanalysis for 12 UTC 1 February 2000. Panel d) is the Remote Sensing Systems TMI 0.25° cloud water path data for 1 February 2000. Black areas denote either land or missing data. ....49

Figure 2.11 Skew-T diagram of the 00 UTC sounding from northern Taiwan for 1 Feb. 2000. (Data courtesy of University of Wyoming.).....50

Figure 2.12 a) Critical number concentrations for the autoconversion of cloud droplets to precipitation for different LWPs as a function of cloud thickness and droplet number concentration using the Kessler-type parameterization of Liu and Daum [2004] and cloud-average LWC as described by equation (3). For autoconversion from cloud droplets to rain droplet to occur, the number concentration must be less than the critical number concentration. b) Layer Average LWC versus cloud thickness for different LWPs. c) As a) but as a function of maximum LWC and not cloud-average LWC. d) Schematic of the liquid water content profile extremes for atypically-thick low marine clouds: uniform profile (grey dashed line) and a linearly increasing profile (black line). ....51

Figure 2.13	The percentage of TMI observations with atypically-thick low marine cloud radiative signatures on a 0.5° by 0.5° grid for 2003 and 2004 combined (top) and the percentage of AMSR-E observations with atypically-thick low marine cloud radiative signatures on a 0.5° by 0.5° grid for 2008 (bottom). The horizontal gray lines at ±40° in the bottom panel are a visual guide to show the limits of the TMI-based plots versus the AMSR-E-based plots. ....	52
Figure 2.14	Average aerosol optical depth at 550 nm based on monthly MODIS-Aqua version 5 data from January 2003 through December 2008. Land areas are masked with the color gray. ....	53
Figure 2.15	The percentage of TMI observations with atypically-thick low marine cloud radiative signatures on a 0.5° by 0.5° grid for each season in 2003 and 2004 combined. ....	54
Figure 2.16	The frequency of TMI observations flagged as atypically-thick low marine cloud as a function of LST, latitude, season, and hemisphere for TMI observations from 2003 and 2004 combined. Local hemisphere winter and summer are represented in the left-hand and right-hand panels respectively (December, January, and February (DJF); June, July, and August (JJA)). ....	55

Figure 3.1 Scatter density plot of clear-sky SST versus Level 2 AMSR-E 89 GHz horizontally polarized brightness temperatures. Clear sky determination is based on 1 degree resolution level 3 Aqua MODIS cloud fraction data where values are less than 1%. Each AMSR-E 89 GHz pixel was assigned a cloud fraction value based on the value of the nearest MODIS cloud fraction pixel. SST values were derived from Remote Sensing Systems 0.25 degree Version-5 AMSR-E Ocean Product. Each AMSR-E 89 GHz pixel was assigned a SST value based on the value of the nearest Remote Sensing Systems SST pixel. The color scale represents the pixel count per bin in all cases.....68

Figure 3.2 Detailed comparison among a) AMSR-E Level 2 Liquid Water Path, b) MODIS Level 2 Cloud Water Path, c) AMSR-E Level 2 89 GHz brightness temperature and d) C-band ship-borne radar data obtained at 1936 UTC on 27 October 2008 in the SE Pacific during VOCALS experiment. The 60 km radius range ring from the radar is overlaid on each image. In order to highlight gradients in LWP, the dynamic range of the color scales differ between a) and b).. .....69

Figure 3.3 Schematic illustrating the difference between 4 and 8 pixels connectivity. 4-Connected pixels are considered adjacent if they

share one their four sides. 8-Connected pixels are considered adjacent if they share a side or a diagonal. ....70

Figure 3.4 Drizzle information for the southeast Pacific on 27 October 2008 at  $\approx 19:35$  UTC. The upper-left panel in AMSR-E horizontally polarized 89 GHz brightness temperature from the L2A product. The middle-left panel is AMSR-E liquid water path from the L2\_Ocean product. The lower-left panel in the Aqua MODIS daytime mean cloud water path from the MYD06\_L2 product. The upper-right panel in the 89 GHz based drizzle detection. The black areas denote drizzle. The middle-right panel is the AMSR-E LWP based drizzle product where drizzle is any area with  $LWP \geq 200$  g/m<sup>2</sup>. The black areas denote drizzle. The bottom-right panel in the Aqua MODIS visible imagery quick-look image ([http://modis-atmos.gsfc.nasa.gov/IMAGES/index\\_myd021km.html](http://modis-atmos.gsfc.nasa.gov/IMAGES/index_myd021km.html)). ....71

Figure 3.5 Histograms comparing drizzle area based on 89 GHz drizzle proxy versus AMSR-E LWP for the region show in Figure 3.4. All areas are in units of number of 89 GHz pixels (6 km  $\times$  4 km). The upper-left panel is the area histogram for 4-connected contiguous drizzle pockets detected using 89 GHz brightness temperature data. The upper-right panel is the area histogram for 8-connected contiguous drizzle pockets detected using 89 GHz brightness temperature data.

The lower-left panel is the area histogram for 4-connected contiguous drizzle pockets defined as contiguous areas with AMSR-E LWP  $\geq 200 \text{ g/m}^2$ . The lower-right panel is the area histogram for 8-connected contiguous defined as contiguous areas with AMSR-E LWP  $\geq 200 \text{ g/m}$ . .....73

Figure 3.6 As Figure 3.4 but for the southeast Atlantic on 26 June 2007 at  $\approx 13:05 \text{ UTC}$ . .....74

Figure 3.6 As Figure 3.4 but for the northeast Pacific on 29 July 2009 at  $\approx 22:00 \text{ UTC}$ . .....76

## **Chapter I - Introduction**

Traditionally, satellite IR data sets have identified low marine clouds based in their cloud top temperature. Low clouds are defined as exclusively liquid phase and often occur as sheets, covering areas of 100s of km for hours to days. This thesis uses satellite passive microwave data sets to address two subtypes of low marine clouds: stratus and stratocumulus clouds that are atypically thick ( $> 2\text{km}$ ) and stratocumulus clouds of more typical thicknesses (500m to 1 km) that contain discrete drizzle cells.

Understanding the characteristics and behavior of low marine clouds is of critical importance for climate research and prediction. Low clouds, as a group, cover a large part of the world's oceans and have a strong effect on the radiation budget and global temperature regulation which has important climate implications. Low marine clouds reflect a large amount of short-wave solar radiation back into space before it can heat the earth's surface. As a result, low marine clouds have a net cooling effect and they are considered to act as a mitigating force against global warming. Currently, low clouds are not well represented in numerical climate models. This known deficiency calls into question the accuracy of the radiative balance in climate models which directly affects the accuracy of predictions of temperature and the impacts of climate change. In order to improve climate predictions, climate models will need to better represent the physical processes behind low marine clouds and their distributions in order to improve predictions of current and future climate [Bony and Dufresne 2005, Bony et al. 2006].

This study addresses deficiencies in the understanding of low marine clouds that has the potential to improve how future climate models handle low marine clouds.

Chapter II explores the existence and characteristics of a subset of low marine clouds with a thickness greater than 2 km. These clouds are herein referred to as atypically-thick low marine clouds. Brightness temperature data from passive microwave sensors were used to identify these clouds. Once identified, data from many sources were used to provide details about the characteristics of the clouds and their background environment. The objectives of this study with respect to atypically-thick low marine clouds were as follows:

- Develop an algorithm using passive microwave data to uniquely identify atypically-thick low marine clouds
- Quantify the spatial and temporal frequency of occurrence of atypically-thick low marine clouds
- Develop a theory on the mechanisms and requirements for the development of atypically-thick low marine clouds that fits observational data of the clouds' characteristics and environment

Chapter III develops a methodology to use 85.5/89 GHz passive microwave brightness temperature data to identify areas of drizzle within marine stratocumulus. Radiative characteristics of marine stratocumulus are closely tied to cloud fraction which in turn is related to albedo. Cloud albedo differs dramatically between regions of continuous unbroken cloud versus regions with mesoscale pockets of open cells [Stevens et al.,

2005]. Observational and modeling studies have implicated drizzle in the formation of pockets of open cells within the closed-cell cloud deck [Stevens et al., 2005; van Zanten and Stevens, 2005; Comstock et al., 2007; Savic-Jovic and Stevens, 2008; Wang and Feingold, 2009]. These studies and more recent observations suggest that drizzle is a necessary but not sufficient condition for the formation of pockets of open cells. Thus, the spatial and temporal distributions of drizzle within marine stratocumulus clouds are key parameters of interest.

85.5/89 GHz brightness temperatures are well suited for use as a drizzle proxy owing to their high resolution and their day-and-night availability. Areas of high liquid water path related to drizzling cloud appear as local maxima in 85.5/89 GHz brightness temperature data when ice is not present. These local maxima in the brightness temperature data were isolated and identified as potential areas of drizzle. Once a drizzle identification methodology is finalized, it can be used to assess the temporal and spatial characteristics of drizzle within marine stratocumulus regions and among different regions. To that end, the objectives of this study concerning the use of 85.5/89 GHz brightness temperature data to identify drizzle in marine stratocumulus were as follows:

- Demonstrate that local maxima in 89 GHz data correspond to high liquid water path values in existing satellite data products
- Demonstrate that local maxima in 89 GHz data correspond to ship-based radar observations of drizzle obtained during the VOCALS field campaign

- Demonstrate that 89 GHz data can be used to identify drizzle in a variety of marine stratocumulus areas
- Demonstrate a proof-of-concept methodology for identifying areas of drizzle from 89 GHz brightness temperature data
- Demonstrate a proof-of-concept methodology for quantifying statistics on drizzle spatial characteristics using algorithms for identifying contiguous-areas in raster data

Chapters II and III are each presented in the form of a discrete journal article.

Chapter II explores the distributions, characteristics, and genesis of atypically-thick low marine clouds. Included in Chapter II is a full contextual introduction, a description of the data and methods used in the study, analysis of the findings, and a discussion of the conclusions and implications of the findings.

Chapter III explores the feasibility of using 85.5/89 GHz brightness temperature data to identify drizzle within marine stratocumulus clouds. Included in that chapter is a brief discussion of the theoretical underpinnings of the method, comparisons of 89 GHz data with related satellite-derived data products for different stratocumulus locations, a proof-of-concept approach for identifying drizzle, and example spatial statistics derived from the drizzle data.

Chapter IV outlines many of the avenues of future research into both atypically-thick low marine clouds and the use of 85.5/89 GHz data in the identification of drizzle within marine stratocumulus.

## **Chapter II – Satellite Observations of Atypically-Thick Low Marine Clouds**

### **2.1. Introduction**

Cloud feedbacks represent the largest feedback component in general circulations models (GCMs) [Colman 2003, Webb et al. 2006, Bony et al. 2006]. The cooling effects attributable to low clouds have an important influence on the regulation and moderation of global temperatures. The representation of feedbacks for low level clouds, including low marine clouds, are shown to be a critical factor in model performance [Yao and DelGenio 2002, Webb et al. 2006, Wyant et al. 2006, Bony and Dufresne 2005]. Zhang et al. [2005] demonstrated that GCMs disagree with International Satellite Cloud Climatology Project (ISCCP) observations on cloud fraction, optical thickness, and cloud-top height illustrating that low marine clouds are not currently well characterized by most GCMs. For GCMs to perform well, they need to accurately characterize the physical properties of low marine clouds and use representative physical or statistical assumptions in cloud parameterizations.

Low marine clouds play an important role in the global radiation budget. Low clouds have a high albedo which allows them to reflect incoming shortwave solar radiation back into space. Low clouds have a cloud-top temperature close to the surface temperature and thus emit a similar amount of outgoing longwave radiation (OLR) as the underlying surface (Stefan–Boltzmann Law). As a result, they re-emit most of the OLR they absorb

and their greenhouse impact is relatively small. As a rule, low clouds have a net cooling effect since they reflect incoming solar radiation and any net greenhouse heating effects are small. Regions where there is a strong net cooling effect due to clouds generally coincide with extensive low cloud cover [Harrison et al. 1990, Hartmann et al. 1992, Klein and Hartmann 1993].

The World Meteorological Organization defines a low cloud as a cloud with a base less than 2 km above the surface. ISCCP defines a low cloud as a cloud with a cloud-top pressure of greater than 680 hPa [Rossow and Schiffer, 1991]. This study will define a low cloud following the ISCCP designation where a low cloud is defined by the height of the cloud top and not the base. Figure 2.1 shows that low clouds occur most frequently off the western coasts of continents and across oceanic baroclinic zones.

Complementing satellite-based cloud climatologies like ISCCP, climatologies of low marine cloud used ship-based cloud observations, coincident surface meteorological observations, and soundings to establish representative relationships between low cloud type and marine boundary layer properties for the subtropics and midlatitudes [Warren et al., 1988; Norris, 1998a; Norris, 1998b; Norris and Kein, 2000]. Relationships among low cloud type, marine boundary layer structure, and surface meteorology differ for different geographical locations and seasons. Fair-weather stratus was shown to be most common over the mid-latitude oceans while ordinary stratocumulus was shown to be most common in the eastern sub-tropical oceans. Fair-weather stratus occurs most commonly in the presence of slight convergence and ascent.

Where previous climatologies of low marine clouds focus on classification based on type, cloud base height, or cloud top height, this study focuses on the thickness of low marine clouds. Specifically, this study focuses on characterizing a subset of low marine clouds that are atypically thick; defined for the purpose of this paper as greater than or equal to 2 km thick. Most GCMs produce low clouds with thicknesses less than 1 km. In an example given by Slingo [1980], low clouds are characterized by a model to be ~750 m (975 – 900 hPa) thick. Baker [1997] uses a thickness of 250 m as a typical value for a marine boundary layer cloud. For the International Cloud Atlas (1956) [Stowe et al. 1988], the tops of low clouds are capped at 2 km by definition. Low marine clouds with a thickness less than 2 km do not represent the entire range of low cloud thicknesses. A proper accounting of low marine cloud must include low clouds thicker than 2 km.

In order to gauge the prevalence and potential impact of atypically-thick low marine clouds, their characteristics and their patterns of occurrence have to be determined.

Section 2.2 defines a methodology for identifying atypically-thick low marine clouds from passive microwave satellite data. Sections 2.3 and 2.4 examine the characteristics, spatial distribution, and temporal distribution of atypically thick low marine clouds using passive-microwave data from the Tropical Rainfall Measuring Mission (TRMM) Microwave Imager (TMI), the Advanced Microwave Scanning Radiometer - Earth Observing System (AMSR-E), the CloudSat Cloud-Profiling Radar, NCEP/DOE model reanalysis, and upper-air soundings. Section 2.5 discusses the relative importance of these clouds.

## **2.2. Data and Methodology**

The primary data used in this study are satellite derived products encompassing microwave band brightness temperature measurements, rainfall estimations, and cloud radar reflectivity profiles. Data from 2003, 2004, and 2008 are used. Passive microwave brightness temperatures are used to radiometrically identify atypically-thick low marine clouds. Active microwave satellite plus ground-based sensors are used to provide additional information when these data are available. For example, cloud radar reflectivity profiles from CloudSat are used to assess the thickness of atypically-thick low marine clouds where they are co-located with AMSR-E observations.

### **2.2.1 TRMM Microwave Imager**

The TMI is a nine-channel passive microwave radiometer whose design is based upon the Special Sensor Microwave/Imager (SSM/I) from the Defense Meteorological Satellite Program. The TMI is carried aboard the TRMM satellite and has an observational domain between 40° N latitude and 40° S latitude. The TRMM satellite makes observations across the full diurnal range. The local time of the TRMM satellite's equatorial crossing repeats with a cycle of 47.5 days [Negri et al., 2002]. The TMI has a rotating offset parabola antenna which scans in a conical pattern with a nadir angle of 49 degrees resulting in an incident angle of 52.8 degrees with the earth's surface. The TMI scans a ground swath 872 km in width (post-boost) [Kummerow et al., 1998].

This study makes use of the TRMM 1B11 version 6 passive microwave brightness temperature and the 2A12 version 6 surface rainfall estimation products. The TRMM

1B11 product contains the calibrated temperature brightness values for each of the TMI's nine channels. Horizontal and vertical polarizations are provided for all channels save 21.3 GHz for which only the horizontal is provided. The values for the channels are split into two groups according to their spatial resolution. The lower resolution channels, consisting of the frequencies 10.65 GHz, 19.35 GHz, 21.3 GHz, and 37 GHz, have half the number of pixels per scan line (104) as the higher resolution 85.5 GHz channels (208 pixels per scan) owing to the larger effective field of view (EFOV) of the lower frequency channels compared to the 85.5 GHz H/V channels.

The TRMM 2A12 product contains derived rainfall and hydrometeor information as calculated by the Goddard Profiling Algorithm (GPROF) [Kummerow et al., 1996; Kummerow et al., 2001]. Included in 2A12 are fields for TMI derived surface rainfall and profiles of precipitation water, precipitation ice, cloud water, cloud ice, and information about the background surface type. This study made use of data concerning surface rainfall information and surface type. Surface rainfall data is provided at the spatial resolution of the 85.5 GHz TMI channels with 208 pixels per conical scan line.

Since TMI brightness temperatures can have a different number of pixels per scan line depending on the frequency of the TMI channel of interest, every other data pixel on a scan line was dropped for the high resolution 85.5 GHz data and the surface rainfall data. This was done to ensure that each conical scan used in the analysis contained the same number of pixels to simplify any processing while still ensuring that all data was

reasonably collocated in space and time. As a result, all TMI orbit-level data used for this study was at a resolution of 104 pixels per conical scan line.

### **2.2.2 AMSR-E**

The Advanced Microwave Scanning Radiometer – Earth Observing System (AMSR-E) is a 12 channel passive microwave radiometer with many sensor characteristics similar to the TMI. AMSR-E is carried aboard the Aqua satellite and has a global observational domain. Aqua is in a sun-synchronous orbit with equatorial overpasses at 01:30 and 13:30 local solar time. Similar to the TMI, the AMSR-E has a rotating offset parabola antenna which scans in a conical pattern with an incident angle of 55 degrees with the earth's surface. AMSR-E flies at an altitude of 705 km and has a swath width of 1445 km. Like the TMI, the EFOV for AMSR-E is different for each channel and is a function of the channel's frequency and the antenna construction. Higher frequency channels have a smaller effective pixel size than lower frequency channels [Kawanishi et al., 2003].

This study makes use of the AMSR-E version 2 Level 2A Brightness Temperature product. This product contains the calibrated temperature brightness values for each of the AMSR-E's twelve channels. Like the TMI 1B11 product, the values for each channel are divided into two groups. The lower resolution channels, consisting of the frequencies 6.9 GHz, 10.7 GHz, 18.7 GHz, 23.8 GHz, and 36.5 GHz, have half the number of points per scan line (243) as the higher resolution 89 GHz channels (486) because they have larger EFOVs compared to the 89 GHz channels.

Just like with the TMI data, every other data point on a scan line was dropped for the 89 GHz AMSR-E brightness temperature data yielding a resolution of 243 points per scan line. All channels were used at their native resolutions. Table 2.1 highlights the relevant characteristics of the TMI and AMSR-E sensors for comparison.

### **2.2.3 Model Reanalysis**

NCEP–DOE Atmospheric Model Intercomparison Project (AMIP-II) reanalysis data [Kanamitsu et al., 2002] was used to provide information about the background and synoptic-scale conditions for specific atypically-thick low marine clouds cases. The reanalysis data is provided four times daily. Wind data at specific pressure levels are provided at a resolution of  $2.5^\circ$  by  $2.5^\circ$  and 2 m temperature data are provided on a T62 Gaussian grid.

### **2.2.4 CloudSat**

CloudSat hosts the first satellite-based cloud radar [Im et al., 2005]. It operates at 94 GHz and can detect reflectivity as low as -29 dBZ. Like the AMSR-E aboard the Aqua satellite, CloudSat is in a sun-synchronous orbit with equatorial overpasses at 01:30 and 13:30 local solar time. CloudSat's cloud-profiling radar is nadir pointing and non-scanning. It covers a swath 1.4 km wide with a vertical resolution of 500 m [Im et al., 2005]. Since CloudSat's cloud-profiling radar is capable of detecting clouds, it can be used to provide a direct measurement of cloud thickness when the radar signal is not strongly attenuated. CloudSat 1B-CPR data files were examined for atypically-thick low

marine clouds where cloud top and cloud base heights were identified. Cloud base heights were subtracted from the cloud top heights in order to estimate cloud thickness.

### **2.2.5 Auxiliary Data**

Level 2 WSR-88D radar data from the NOAA National Climatic Data Center and the Central Weather Bureau of Taiwan for several coastal radar locations was processed for comparison to TRMM products. The radar data was processed through a quality control program to remove some non-meteorological echoes as well as noise. The data was then interpolated to a 240 km by 240 km Cartesian grid with 3 km horizontal resolution and 3 km vertical resolution. Radar echo spatial distribution and intensity were compared to the spatial distribution and rain rate intensity for satellite-derived surface rainfall fields.

Upper-air sounding data retrieved from the University of Wyoming online sounding archive was used to examine the thermodynamic profiles at several coastal locations for near-shore cases of atypically-thick low marine cloud. The relative humidity information was used to estimate the cloud base and cloud top.

### **2.2.6 Identifying Atypically-Thick Low Marine Clouds**

To find a unique identifying signature for atypically-thick low marine clouds, the passive microwave brightness temperatures from the TRMM 1B11 product were examined for a set of training cases of atypically-thick low marine cloud events confirmed via analysis of satellite, coastal S-band radar data, and upper-air sounding data. These cases are summarized in Table 2.2. The joint brightness temperature distribution among seven passive microwave channels - 10V, 19V, 19H, 21V, 37V, 37H, and 85.5V - is used to

distinguish atypically-thick low marine clouds from a clear ocean background and other cloud and precipitation features. For a given passive microwave pixel to be flagged as atypically-thick low marine cloud, the set of brightness temperatures for that pixel must lie between specified ranges that differ for each of the seven channels used in the search algorithm. Non-oceanic pixels (i.e. land and coast) are not examined. Table 2.3 summarizes the filtering criteria used by the search algorithm. The tuning of the search algorithm was completed by examining training cases until the range of brightness temperatures associated with atypically-thick low marine cloud for each channel stabilized.

Figure 2.2 depicts the joint distributions of brightness temperatures for all the vertically-polarized channels used to classify atypically-thick low marine clouds. Some channel's brightness temperatures for atypically-thick low marine clouds are well correlated while others are not. To minimize the problem of the misidentification of mixed-phased marine clouds as atypically-thick low marine clouds, a bounded linear relationship between the 19V and the 21V channels was imposed as enumerated in Table 2.3. Figure 2.3 illustrates an example of an atypically-thick low marine cloud case in the Florida Strait and shows the cloud boundaries along with the associated brightness temperatures for the vertically polarized channels used in the search algorithm.

One month's worth of individual orbit files were processed at a time. Pixels in each orbit identified as atypically-thick low marine cloud were sorted into  $0.1^\circ$  by  $0.1^\circ$  boxes. For a given  $0.1^\circ$  by  $0.1^\circ$  box, each atypically-thick low marine cloud pixel was counted and, at

the end of the monthly computational period, the total number of observed atypically-thick low marine cloud pixels was divided by the total number of TMI pixels for that box yielding a map of the normalized percentage of TMI observations having a radiative signature similar to atypically-thick low marine cloud.

In the initial testing, the search algorithm was occasionally flagging scattered pixels around the edges of deeper convection as atypically-thick low marine clouds. Since atypically-thick low marine clouds are known to primarily occur in relatively large continuous sheets (section 2.3), an area-based spatial filter was added to the algorithm. A contiguous area-based filtering technique was implemented to filter out all groups of pixels with a contiguous area below  $50\ 0.1^\circ \times 0.1^\circ$  pixels. A standard 4-connected contiguous area search algorithm for raster data [Rosenfeld and Pfaltz, 1966; Haralock and Shapiro, 1992] is used to find contiguous areas of atypically-thick low marine clouds on a per orbit basis. Figure 2.4 illustrates how the area-based filter criterion removes erroneously flagged pixels in the vicinity of Tropical Depression Jove. Since the pixels flagged by the search algorithm based on their radiances do not meet the minimum contiguous area criterion, they are removed from the set of pixels identified as atypically-thick low marine cloud. This area-based filtering technique expands the analysis from a pixel-based framework to a feature-based framework where the broad spatial characteristics of the desired phenomenon are evaluated. While such techniques are not unique, they represent an under-utilized class of techniques in the meteorological satellite data analysis field.

The filtering criteria described above were also applied to AMSR-E data by substituting the 24V and 89V AMSR-E channels for the 21V and 85.5V TMI channels. The same brightness temperature ranges are used despite the slight differences in frequencies between the AMSR-E and TMI. The TMI and AMSR-E center frequencies, viewing geometry, spatial resolution, and calibration are close but do not exactly match. The atypically-thick low marine clouds search algorithm uses ranges of brightness temperature values from several channels combined with spatial continuity. This combination of criteria decreases sensitivity to exactly matching the sensors' center frequencies and spatial resolutions. Table 2.2 lists the training cases used in the development of the atypically-thick low marine cloud search algorithm.

### **2.2.7 Using the Search Algorithm with AMSR-E to Find Relevant CloudSat Data**

The Aqua satellite and CloudSat are both part of the A-Train satellite constellation. Sensors aboard both satellites make nearly-concurrent observations of the same locations [Stephens et al., 2002]. For the purposes of this study, we are interested in the fact that AMSR-E observations have a corresponding CloudSat observation only a few minutes behind. We used the search algorithm on AMSR-E data to identify likely atypically-thick low marine clouds concurrently observed by CloudSat. CloudSat's CPR is able to provide more information about cloud thickness than operational upper-air soundings since upper-air balloon launches typically occur twice per day and don't have good coverage over the open oceans.

Subsets of atypically-thick low marine clouds, identified via AMSR-E, with corresponding CloudSat observations were flagged. The CloudSat reflectivity profiles for these cases were examined to determine the distributions of cloud base, top, and thickness.

### **2.3. Examples of Atypically-Thick Low Marine Clouds**

The following subsections examine individual occurrences of atypically-thick low marine clouds. Satellite data, upper-air sounding data, and model reanalysis data are combined in order to investigate the environmental conditions under which these clouds occur and to deduce associated physical processes.

#### **2.3.1 Advection Fog Genesis**

Figure 2.5 illustrates an example of atypically-thick low marine clouds over the Southeast Pacific Ocean around 00:02 UTC (middle-afternoon) on 29 August 2008. In this case, we infer that the atypically-thick low marine clouds over the Southeast Pacific Ocean derive their origin from advection fog as a result of the advection of warm moist air over cool water. Panel a of Fig. 2.5 illustrates the subset of clouds identified as atypically-thick low marine clouds. Only a small fraction of the cloud sheet is classified as atypically-thick low marine cloud.

The CloudSat vertical reflectivity data in panel b of Figure 2.5 is qualitatively similar to schematics of open ocean warm fronts in the literature where warm moist air moves along a warm front over a region of cold air [e.g. Harrold 1973]. The cloud area classified

as atypically-thick low marine cloud is in the warm sector and CloudSat data indicates that it had a thickness of approximately 3 km. The reflectivity values indicated by CloudSat within the red box do not indicate any notable precipitation that would be above the minimum threshold detectable by passive microwave instruments ( $\sim 0.5$  mm/hr).

The 925 hPa winds from the NCEP/DOE model reanalysis for 00 UTC on 29 August 2008 were northerly and strong with wind speeds in excess of 25 m/s. The corresponding satellite-based sea surface temperature measurements indicated a cold ocean surface with a temperature on the order of  $5^{\circ}$  C in the vicinity of the low clouds. The 2m surface temperature data from the NCEP/DOE model reanalysis for 00 UTC on 29 August 2008 were between  $10^{\circ}$  and  $12^{\circ}$  C. The northerly winds were facilitating low-level warm air advection. Comparing the 2-meter temperature with the SSTs shows that there was a temperature differential of  $\sim 5^{\circ}$  C for the low cloud area corresponding to the CloudSat overpass. Modeling studies by Oliver et al. [1978] and Koraćin et al. [2001] produce advection fog with a temperature differential between the sea surface and overlying air of  $3^{\circ}$  C or less.

Figure 2.6 illustrates the relevant physical processes theorized to act in the generation of atypically-thick low marine clouds in this case over the Southeast Pacific Ocean. Warm-air advection over cold water typically leads to advection fog. The cold water cools the near-surface air to saturation causing condensation and fog formation. Reanalysis data show strong wind speeds that should act to prevent strong stratification and allow the cloud layer to grow via continual condensation at or near the surface. Previous studies of

advection fog off the coast of California demonstrate how turbulent mixing at the cloud top mixes moisture upwards, thereby raising the top of the cloud [Oliver et al., 1978; Noonkester, 1979; Koračin et al., 2001]. At the top of the cloud, radiative cooling and evaporational cooling due to dry-air entrainment generate instability that fuels mixing [Oliver et al. 1978, Noonkester 1979, Koračin et al. 2001, Gerber et al. 2005]. Cooling at the top of the cloud layer acts in concert with condensation at the bottom of the cloud layer to generate sufficient instability for the redistribution of moisture throughout the cloud layer. This mixing maintains the distribution of moisture necessary to prevent the erosion of the cloud layer due to dry-air entrainment or droplet fallout.

### **2.3.2 Steam Fog Genesis**

Figure 2.7 illustrates an example of atypically-thick low marine clouds over the Gulf of Mexico in the early afternoon on 3 January 2008. This case, like the Southeast Pacific Ocean case from section 2.3.1, is inferred to have originated from fog. However, unlike the Southeast Pacific Ocean case, we inferred that the Gulf of Mexico case originated as steam fog that formed with the advection of cool air over warm water. Panel a of Fig. 2.7 illustrates the subset of clouds identified as atypically-thick low marine clouds by the algorithm described in section 2.2. The clouds occur in a continuous sheet and are several hundred kilometers in extent along any given direction.

CloudSat vertical reflectivity profiles for the Gulf of Mexico area shows that the clouds identified as atypically-thick have cloud top heights of 2.5 km with the base of the clouds extending to the surface. The reflectivity values for the cloud sheet are consistently below

0 dBZ and do not suggest any notable surface precipitation. The clouds appear to be horizontally uniform save for some quasi-cellular features, consistent with other studies of the structure of stratiform marine clouds and fog [Atkinson and Zhang, 1996; Hamazu et al., 2003]. Visible MODIS data from Aqua show roll clouds over the Gulf of Mexico that transition into a tightly packed closed-cell structure indicative of cold air overrunning warm water [Atkinson and Zhang, 1996].

The 925 hPa winds from the NCEP/DOE model reanalysis for 18 UTC on 3 January 2008 were from the northeast with some low-level speed-induced convergence in the Gulf of Mexico north of the Yucatan Peninsula. Satellite-based sea surface temperature measurements, also from 18 UTC, indicated a relatively warm ocean surface with temperatures ranging from 23° to 27° C in the vicinity of the low clouds. The 2 m surface temperature data from the NCEP/DOE model reanalysis shows that the near-surface air temperatures were between 15° and 25° C. The northeast winds facilitated low-level cold air advection. National Buoy Data Center information for buoy number 42001 in the Gulf of Mexico under the low marine clouds shows that the air temperature was 10.1° C colder than the water temperature. Such a temperature differential favors latent and sensible heat fluxes that would provide low-level moisture and heat to drive unstable mixing. The moisture would allow for the generation of clouds and the thickening of existing clouds via lowering of the lifting condensation level. Cloud water path values are on the order of 0.3 to 0.5 kg/m<sup>2</sup>.

Figure 2.8 illustrates the relevant physical processes inferred to act in the generation of atypically-thick low marine clouds in this case. The advection of air cooler than the water leads to steam fog. Moisture flux causes the cooler air near the surface of the water to saturate, generating “steam plumes” which have been described as vertically-oriented tubes of visible condensate [Grossman and Betts 1990]. The cold-air advection provides a constant supply of cool, near-saturated air and the warm water provides a constant supply of moisture so that the generation of steam plumes can be maintained. Convective mixing, fueled by sensible heat flux and condensational warming near the surface, transports moisture upwards in the associated cloud-topped mixed layer above the lifting condensation level, forming clouds. This mixing also acts to lift saturated air away from the surface so that the heat flux is maintained. The long duration of the latent heat flux causes the cloud layer to thicken both as the convective mixed layer increases in height and as the LCL lowers due to the moisture introduced in the sub-cloud region. As was mentioned in section 2.3.1, turbulent mixing at the top of the clouds acts to increase the height of the cloud by transporting moisture above the top of the cloud. This turbulent mixing is fueled primarily by radiational cooling, evaporational cooling due to dry-air entrainment, and wind shear. Heating at the bottom of the cloud and cooling at the top of the cloud fuel mixing within the cloud, keeping moisture well distributed.

An example of steam fog growing into a thick low cloud in a situation with a large contrast between the air and sea temperature was observed during the Genesis of Atlantic Lows Experiment (GALE). Aircraft observed steam fog developing into a low marine cloud approximately 2 km thick on 28 January 1986 over the western edge of the Gulf

Stream off the coast of North Carolina [Grossman and Betts 1990]. In that event, the sea-air potential temperature difference was observed to be 23° C. Atkinson and Zhang [2006] described clouds forming via steam fog from cold air outbreaks with air/sea temperature differences ranging from 0.5° C to 12° C. However, many of those events did not develop low marine clouds with thickness > 2 km. Clouds with a thickness of up to 3.2 km were listed by Atkinson and Zhang [2006, Table 2.1], but air/sea temperature differences were not reported in any of the cases where the cloud thickness was above 2 km. While a significant difference between air and sea temperature is required for steam fog, such a contrast is not solely sufficient for atypically-thick low marine clouds development.

### **2.3.3 Steam Fog over East China Sea**

Berg et al. [2006] (hereafter B06) investigated the differences in rainfall detection between the PR and TMI. Their study noted a large area of discrepancy between the TMI and PR over the East China Sea where the TMI was frequently signaling rain when the PR was not. B06 inferred that aerosol loading suppressed precipitation in the clouds over the East China Sea. Their analysis was based on the 1st indirect effect [Twomey 1974, 1977] where a polluted cloud will have a greater number of smaller droplets than a non-polluted cloud with the same liquid water content. B06 offered some calculations as a proof-of-concept approach to support the plausibility of their hypothesis based on observations of droplet number concentration from Ishizaka et al. [2003]. They suggested that for a relatively high liquid water path cloud (1 kg/m<sup>2</sup>) with a plausible cloud droplet

number concentration based on observations of polluted clouds ( $400 \text{ cm}^{-3}$ ), the reflectivity could be reduced to approximately 18 dBZ – just below the PR minimum threshold of detection. The case examined by B06 is shown in Figure 2.9. There was a large area of precipitation indicated by the TMI that was not present in the corresponding PR observation. The majority of the area flagged as raining by the TMI was flagged as atypically-thick low marine cloud by our algorithm. Examination of the coastal S-band radar data for this case did not reveal a widespread area of precipitation corresponding to the TMI rainfall area. The reflectivity range corresponding to the TMI rain rates as calculated by B06 ( $\sim 18 \text{ dBZ}$ ) would be observable by the coastal S-band radar if the echoes were present. The operational minimum detection threshold for the Taiwan radar is 5 dBZ or less in VCP 21 precipitation mode depending on beam elevation and range [Miller et al., 1998]. The Taiwan coastal S-band WSR-88D radar did not detect any echoes  $> 10 \text{ dBZ}$  in the East China Sea corresponding to features identified as raining by the TMI but not PR. The radar observations do not rule out that aerosols may be a contributing factor, but support the conclusion that aerosols are not a major contributor to atypically-thick low marine clouds in the B06 case.

Figure 2.10 shows the Remote Sensing Systems  $0.25^\circ$  TMI Cloud Water Path data for these clouds and indicates a peak value of  $0.54 \text{ kg/m}^2$ . B06 indicated LWP for the same region as  $\sim 0.5\text{-}1.2 \text{ kg/m}^2$ . Either the  $\text{LWP} = 1.2 \text{ kg/m}^2$  occurred over a small area below the resolution of the RSS LWP product or it is an overestimate. Based on the nearby Taipei, Taiwan sounding, these clouds were  $\sim 2.75 \text{ km}$  thick (950 hPa to 700 hPa, Figure 2.11). B06 chose a cloud thickness of 1.5 km to characterize the clouds in their study; a

value much too low. The combination of underestimating cloud thickness and overestimating LWP yielded an erroneously high LWC in their calculations.

Similar to the Gulf of Mexico example, the conditions for steam fog were present in this case. Figure 2.10 depicts the 1000 hPa winds from the NCEP/DOE model reanalysis for 12 UTC on 1 February 2000, satellite-based sea surface temperature, and model reanalysis 2 m surface temperatures. The 1000 hPa low-level winds were from the north and northeast. Satellite-based sea surface temperature measurements indicate ocean surface temperatures ranging from 14° to 20° C off the northern coast of Taiwan. Off the northeastern coast, there was a sharp gradient in SST where the ocean temperature jumped to 24° C. The near-surface air temperatures were between 10° and 15° C according to 2 m surface temperature data from the NCEP/DOE model reanalysis. The northeasterly winds are facilitating low-level cold air advection. Comparing the 2-meter temperature with the SST data shows that there is a temperature differential ranging from 5° to 10° C north of Taiwan. As in the Gulf of Mexico example, there was a significant temperature differential where cool air was being advected over warm water. This facilitated sensible and latent heat fluxes, providing low-level moisture and instability allowing for the generation of clouds and the lowering of the LCL for existing clouds, leading to an increase in their thickness. We infer that the advection fog built into a layer of low stratiform marine cloud with a thickness of 2.75 km as reflected in local sounding data (Fig. 2.11).

Finally, this case off the north coast of Taiwan had an unphysical TMI-retrieved hydrometeor profile. This can be seen in other atypically-thick low marine clouds cases as well. Sounding data in Figure 2.11 indicates a cloud top of 3.9 km and an overall cloud thickness of 2.75 km. However, as in other cases with low cloud, the TMI indicated a layer of ice-phase cloud droplets above the observed cloud top all the way to the top of the troposphere (Figure 2.9d). The incorrect hydrometeor profile is an indication that the TMI algorithm is providing an incorrect physical interpretation of the observed clouds and may be making incorrect assumptions about their characteristics and structure.

### 2.3.4 Moisture Profiles

The relationship between LWP, cloud thickness, and layer-averaged liquid water content can be expressed by the formula

$$\overline{LWC} = \frac{LWP}{\Delta Z} \quad (2.1)$$

where  $\overline{LWC}$  is the layer average liquid water content in  $\text{g/m}^3$ , LWP is the liquid water path in  $\text{kg/m}^2$ , and  $\Delta Z$  is the cloud thickness in km.

Atypically-thick low marine cloud may fool passive-microwave rain rate retrievals such as the TMI and other Goddard profiling algorithm-based products into indicating rain if the observed LWP is erroneously associated with a cloud that is thinner than the actual cloud. The Goddard profiling algorithm's rain/no-rain threshold is partially based on measurements of the liquid water path (LWP) [Kida et al., 2009]. For the same LWP, a thicker cloud will spread the same amount of water over a larger volume resulting in a

lower layer-averaged liquid water content (LWC) than for a thinner cloud.

Autoconversion of cloud droplets into rain is usually described as a function of droplet concentration ( $N_d$ ) and drop radius but can equivalently be described as a function of droplet concentration  $N_d$  and LWC (Liu et al. 2004; from their eqn. 6).

$$N_{\text{crit}} \sim 24.63^2 \text{LWC}^{4/3} \quad (2.2)$$

where  $N_{\text{crit}}$  is the critical droplet number concentration for autoconversion and LWC is the liquid water content.  $N_{\text{crit}}$  is referred to as the critical number because autoconversion occurs whenever cloud  $N_d$  is less than  $N_{\text{crit}}$ . Using equations (2.1) and (2.2), given the observed natural range of  $N_d$  and LWP, one can determine LWC values below which autoconversion will not occur.

Stratiform clouds generally have a LWC profile that starts near zero and increases linearly with height [Oliver et al., 1978; Frisch et al., 1995; Hayasaka et al., 1995; Hogan et al., 2005]. Since the profile is linear,  $\overline{\text{LWC}}$  is equal to half the maximum LWC ( $\text{LWC}_{\text{max}}$ ) for the linear profile. A uniform LWC profile and a linear LWC profile represent limiting cases for stratiform clouds (Figure 2.12 panel d). Actual atypically-thick low marine cloud LWC profiles should be somewhere between these two extremes.

Figure 2.12 uses equations (1) and (2) to show the critical droplet number concentration versus the cloud thickness for different LWP values using either a uniform LWC profile (panel a) or a linear LWC profile (panel c). Precipitation will occur for a given LWP when the cloud droplet number concentration is less than the critical value at the relevant

cloud thickness coordinate. For a given cloud thickness, the critical cloud droplet number concentration is higher for a cloud with a higher LWP (and higher LWC) value.

Observations made during the Asian Particle Environmental Change Studies and described by Ishizaka et al. [2003] state that “clean” clouds have a number concentration around  $150 \text{ cm}^{-3}$  and polluted clouds have a number concentration around  $400 \text{ cm}^{-3}$ . We first assume a LWP of  $1 \text{ kg/m}^2$  which is on the higher end of observations of clouds we have identified as atypically thick low marine clouds. Table 2.4 summarizes the relevant values for a LWP of  $1 \text{ kg/m}^2$  and a cloud thickness of 1.5 km versus 3 km.

This table illustrates that the only condition where the 1.5 km thick cloud with a LWP =  $1 \text{ kg/m}^2$  will not undergo autoconversion is when the air is polluted and  $\overline{\text{LWC}} = 0.67 \text{ g m}^{-3}$  is representative of the LWC in the cloud. In contrast, autoconversion will not take place in the thick cloud in the polluted case independent of whether one uses  $\overline{\text{LWC}}$  or  $\text{LWC}_{\text{max}}$  as the representative value. Autoconversion will occur if the  $\text{LWC}_{\text{max}}$  of 0.67 is the representative value and the air is clean. The key point is that autoconversion will not take place in low LWC (e.g.  $0.33 \text{ g m}^{-3}$ ) cloud regardless if it is polluted or not. Hence, processes that reduce the LWC by dispersing the cloud water over a deeper layer act to suppress precipitation. We propose that such processes are active in regions with atypically thick low marine clouds.

## **2.4. Global Distribution of Atypically-Thick Low Marine Clouds**

Global maps, calculated and compiled using the methods described in Section 2.2, provide information about the spatial distribution and the temporal frequency of atypically-thick low marine cloud. TMI data were used to investigate atypically-thick low marine clouds across a full diurnal range. AMSR-E data provided coverage at high latitudes. For illustrative purposes, we used TMI observations for 2003 and 2004 (mild El Niño), and AMSR-E observations for 2008 (mild La Niña). AMSR-E data from 2008 were used so that coincident CloudSat data could also be examined.

### **2.4.1 Annual Patterns**

The top panel of Fig. 2.13 shows the percentage of TMI observations with atypically-thick low marine cloud radiative signatures on a  $0.5^\circ$  by  $0.5^\circ$  grid for 2003 and 2004 combined. In the TMI data, atypically-thick low marine cloud signatures have a conditional average annual occurrence rate of 0.3% globally, but localized regions can have an annual frequency as high as 6%. Higher frequencies occur off the eastern coast of China northwest of Taiwan, off the US Atlantic coast, in the western Gulf of Mexico, and in the southern Pacific and Atlantic oceans. Atypically-thick low marine clouds are conspicuously absent in the tropics at latitudes closer than  $15^\circ$  from the equator.

The Aqua satellite, which carries the AMSR-E sensor, is in a solar synchronous orbit with an equatorial crossing time of 01:30 LST and 13:30 LST. As a result, AMSR-E does not provide the same diurnal coverage as TMI. The bottom panel of Fig. 2.13 shows the percentage of AMSR-E observations with atypically-thick low marine cloud radiative

signatures on a  $0.5^\circ$  by  $0.5^\circ$  grid for 2008. The annual plot of the percentage of AMSR-E observations with atypically-thick low marine cloud radiative signatures shows that these clouds extend poleward beyond the confines of the TMI observational domain to latitudes greater than  $60^\circ$ . Comparing the AMSR-E data with the TMI reveals that the TMI panel shows much higher frequency of atypically-thick low marine cloud observations. One main cause of the discrepancy is that the AMSR-E data does not cover the full diurnal range like the TMI and, as a result, there are differences due to diurnal variation. Also, the search algorithm is not as finely tuned for the AMSR-E as the TMI. Differences in the satellite altitudes, sensor view angles, and channel centers between the TMI and AMSR-E instruments can create differences in the results when the same search algorithm is applied to each sensor. Nevertheless, in the geographic regions for which the AMSR-E and the TMI observational domains overlap, the relative spatial distribution of atypically-thick low marine clouds is similar. Both sensors identify the same areas with the highest frequencies of occurrence.

Figure 2.14 depicts the average Aerosol Optical Depth for 2003 through 2008.

Atypically-thick low marine clouds occur in areas with different levels of aerosol pollution, ranging from polluted areas (e.g. East China Sea) to areas with very low aerosol amounts (e.g. Southern Pacific Ocean). The variety of background aerosol environments where these clouds occur implies that aerosols are not the sole cause of the occurrence of atypically-thick low marine clouds.

### **2.4.2 Seasonal Patterns**

The distribution of atypically-thick low marine clouds exhibits a strong seasonal cycle that differs between the northern and southern hemisphere for a given season. Figure 2.15 depicts the percentage of TMI observations with atypically-thick low marine cloud radiative signatures on a  $0.5^\circ$  by  $0.5^\circ$  grid for each three-month season using data from 2003 and 2004. In both hemispheres, atypically-thick low marine clouds are most common during their local winter which is consistent with an origin related to cold-air outbreaks. In the northern hemisphere, atypically-thick low marine clouds hardly occur at all during the summer. In contrast, for the southern hemisphere, atypically-thick low marine clouds are present during local summer, but occur less frequently than in the winter months. On a seasonal basis, the highest frequency of occurrence of atypically-thick low marine clouds occurs in the East China Sea during local winter where  $\sim 10\%$  of TMI observations have their radiative signature. During the local summer, atypically-thick low marine clouds were not observed in the East China Sea. Peak frequencies of occurrence of atypically-thick low marine clouds do not exceed 5% for any  $0.5^\circ$  by  $0.5^\circ$  grid in any season in the southern hemisphere in either the TMI or AMSR-E domains.

### **2.4.3 Diurnal Patterns**

Figure 2.16 depicts the frequency of TMI observations with atypically-thick low marine cloud radiative signatures as a function of season, hemisphere, and LST. The pixel frequency sum is the sum of the percent frequency of occurrence at a given local time for each  $0.5^\circ$  by  $0.5^\circ$  pixel in the northern or southern hemisphere and is normalized for

ocean area in each hemisphere. For the local summer, neither hemisphere demonstrates a clear diurnal maximum or minimum in the occurrence of atypically-thick low marine clouds. For the local winter, both the southern and the northern hemispheres show a stronger diurnal pattern. The northern hemisphere winter has a peak in the occurrence of atypically-thick low marine clouds in the late afternoon near 17 LST and a minimum in the early morning hours. The southern hemisphere winter has a broad peak in the occurrence of atypically-thick low marine clouds in the early through late afternoon and an equally broad minimum in the pre-dawn to early morning hours. While there is a signal of some diurnal influence on the frequency of occurrence of atypically-thick low marine clouds, variations at the seasonal scale are much more pronounced.

## **2.5. Conclusions**

Atypically-thick low marine clouds are low stratiform marine clouds with a thickness greater than 2 km that occur in large continuous sheets, usually tens to hundreds of kilometers across, and do not produce rain  $> 0.4 \text{ mm hr}^{-1}$  (i.e. the TMI minimum detectable threshold). In this study we examined the spatial, temporal, and diurnal distributions of atypically-thick low marine clouds using multiple years of passive microwave satellite data. Additionally, we examined specific examples of atypically-thick low marine clouds to characterize the clouds' properties and background environment in order to infer information about their formation.

In examining cases of atypically-thick low marine clouds over the Gulf of Mexico and the Southeast Pacific, two potential formation mechanisms were inferred based on the

environmental background data: steam fog/cold air outbreak genesis and advection fog/warm front genesis. These clouds occur in regions without a strong capping inversion. Mixing processes deepen the cloud layer and disperse the vertically-integrated liquid water content over a longer path, reducing the volumetric liquid water content. Atypically-thick low marine clouds occur most commonly in the winter hemisphere on the lee side of continents at latitudes between  $15^\circ$  and  $60^\circ$  from the equator. For localized regions, upwards of 30% of monthly and 10% of annual TMI observations can have atypically-thick low marine cloud radiative signature. These clouds occur most frequently off the eastern coast of China northwest of Taiwan, the southern Atlantic and Pacific Oceans, the western Gulf of Mexico, and over the Gulf Stream and Kuroshio currents (Fig. 2.13). In ocean regions with a nearby continent, these clouds appear to be associated with cold air outbreaks over warm SSTs (steam fog), but they can also occur over open ocean associated with extratropical cyclones (advection fog).

The geographic regions where atypically-thick low marine clouds occur have different levels of aerosol pollution, ranging from very polluted areas (e.g. East China Sea) to areas with very low aerosol amounts (e.g. Southern Pacific Ocean). The appearance of atypically-thick low marine cloud in both high and low aerosol regions discredits the theory proposed in Berg et al. (2006) that aerosols are a necessary ingredient in the formation of low marine clouds with a large LWP. Aerosols may at times play a role the development of atypically-thick low marine clouds but they are not a required factor. Examination of the droplet autoconversion threshold, as formulated by Liu et al. [2004] and Liu and Daum [2004], suggests that aerosol suppression of precipitation is a moot

point in many cases for atypically-thick low marine cloud since LWC is sufficiently low such that conditions for precipitation formation are not met regardless if the air is clean or polluted. Sorooshian et al. [2009] examined how aerosols act to reduce rain rate in clouds with observed rain rates greater than 1 mm/hr and LWP values between 0.5 and 1kg/m<sup>2</sup>. Those results do not apply to atypically-thick low marine clouds since they do not precipitate and, thus, are not a part of the set of clouds Sorooshian et al. examined.

The diurnal patterns of atypically-thick low marine clouds vary with season and are different between the northern and southern hemispheres. The difference between the two seasons is much more pronounced in the northern hemisphere than in the southern hemisphere. This may be related to a higher prevalence of the cold air outbreak genesis for these clouds in the northern hemisphere. For both the northern and southern hemispheres, the strength of the diurnal cycle of atypically-thick low marine cloud occurrence is stronger in local winter. The peak diurnal occurrence of atypically-thick low marine cloud occurs between local noon and sunset in both hemispheres. In all cases, the seasonal variability in the occurrence of atypically-thick low marine clouds is more pronounced than the diurnal variability.

Our understanding of the climate system, and by extension, our ability to predict it, is tied to how we understand and are able to characterize low marine clouds. GCM performance is critically related to the quality of low cloud characterization [Yao and DelGenio 2002]. Many GCMs do not characterize the full range of characteristics of low marine clouds, including cloud thickness [Slingo 1980; Baker 1997]. Passive-microwave-derived

information about low marine clouds – atypically-thick low marine clouds in particular – allows for a broader and more encompassing means of classification for low marine clouds by subdividing low clouds into subcategories by thickness. Passive-microwave sensors are well suited to such tasks since they cover a much larger swath than the cloud profiling radar aboard CloudSat. Atypically-thick low marine clouds can then be identified, studied, and accounted for in climatologies and models. Avenues for future research include how the evolution of atypically-thick low marine clouds differs compared to thinner, more typical marine stratus.

## Chapter II - TABLES

**Table 2.1. Comparison and TRMM versus AMSR-E Characteristics and Features**

Feature	TRMM	AMSR-E
Channels (GHz)	10.7 H&V, 19.4 H&V, 21.3 V, 37 H&V, 85.5 H&V	6.9 H&V, 10.7 H&V, 18.7 H&V, 23.8 H&V, 36.5 H&V, 89 H&V
Instantaneous Field of View	[69 km x 41.8 km]-[7.7 km x 4.7 km]	[74 km x 43 km]-[6 km x 4 km]
Domain	40° N - 40° S Latitude	Global
Overpass Time	Variable	13:30 LST (equator)

*H and V denote horizontal and vertical polarizations respectively.*

**Table 2.2. Atypically-Thick Low Marine Clouds Training Cases**

Sensor	Area of Interest	Orbit #	Date	Est. Thickness (km)
TMI	East China Sea	12547	1 Feb 2000	2.75
TMI	East China Sea	23868	21 Jan 2002	
TMI	East China Sea	23971	27 Jan 2003	
TMI	East China Sea	24036	1 Feb 2002	3
TMI	East China Sea	24047	1 Feb 2002	3
TMI	Gulf of Mexico	24533	5 Mar 2002	3
TMI	Gulf of Mexico	24548	5 Mar 2002	3
TMI	NW Atlantic	41824	18 Mar 2005	3.25
AMSR-E	Gulf of Mexico	NA	3 Jan 2008	2.5
AMSR-E	SE Pacific	NA	29 Aug 2008	3

**Table 2.3. Summary of Atypically-Thick Low Marine Cloud Filtering Criteria**

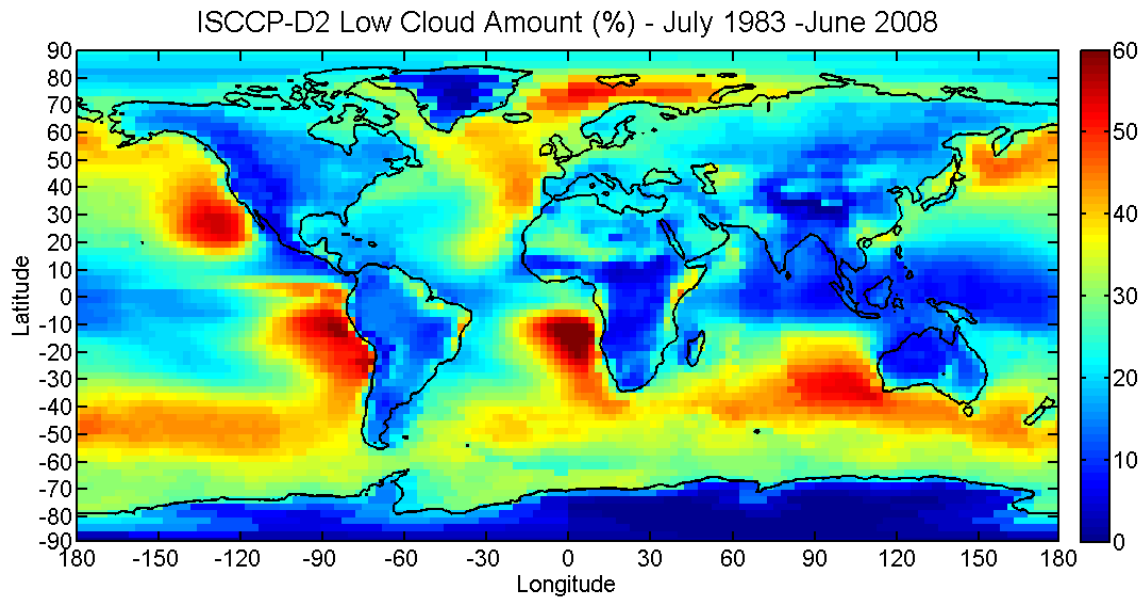
Criteria	Filter Range
10 GHz V	170 K – 185 K
19 GHz V	195 K – 225 K
19 GHz H	130 K – 175 K
21/23 GHz V	210 K - 242 K
21/23 GHz V	$1.45 \cdot 19V - 75 \pm 8$ K
37 GHz V	230 K – 254 K
37 GHz H	185 K – 130 K
85/89 GHz V	268 K – 280 K
Contiguous Area	>50 0.1° by 0.1° boxes

*“V” denotes vertical polarization. TMI channel frequencies precede AMSR-E frequencies where they differ (i.e. TMI/AMSR-E).*

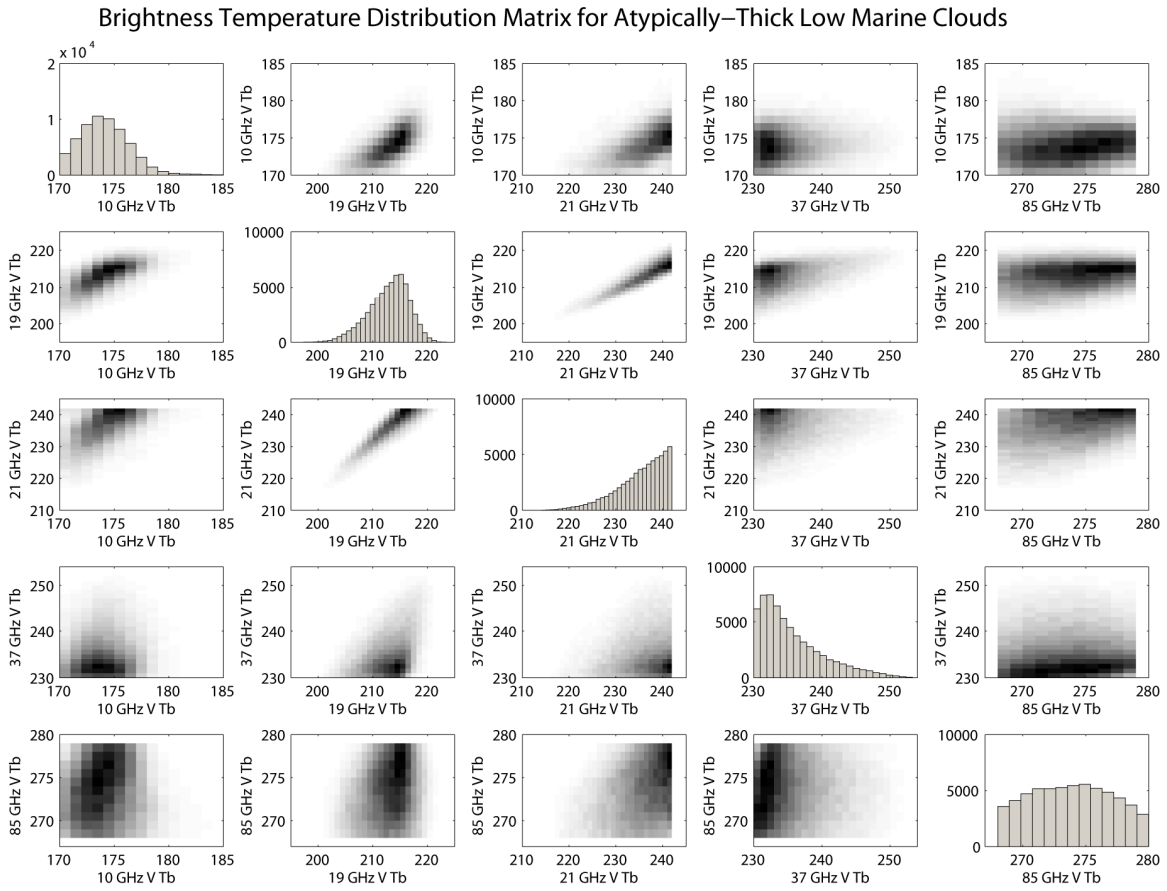
**Table 2.4. Autoconversion threshold criteria for example cases**

	Ncrit (cm <sup>-3</sup> )	Autoconversion if N=400 (polluted)	Autoconversion if N=150 (clean)
Cloud thickness = 1.5 km			
Layer average LWC=0.67 g m <sup>-3</sup>	353	No	Yes
Potential maximum LWC = 1.3 g m <sup>-3</sup>	890	Yes	Yes
Cloud thickness = 3 km			
Layer average LWC=0.33 g m <sup>-3</sup>	140	No	No
Potential maximum LWC=0.67 g m <sup>-3</sup>	353	No	Yes

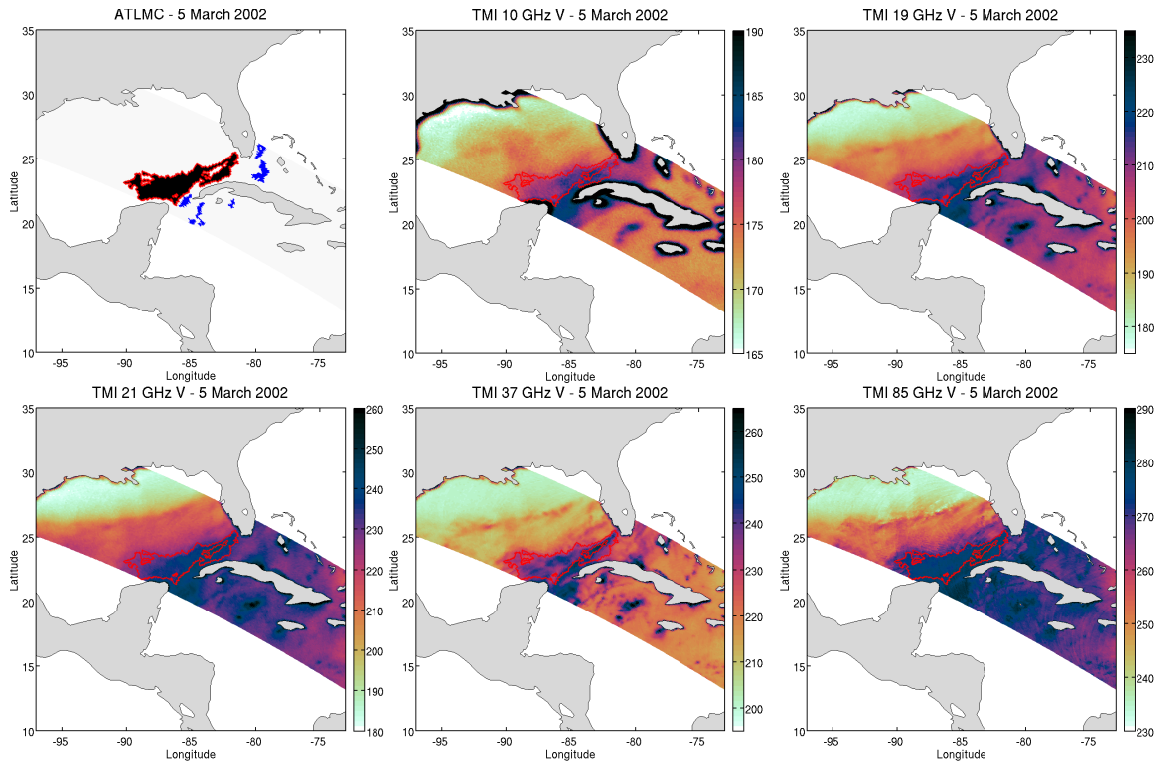
## Chapter II - FIGURES



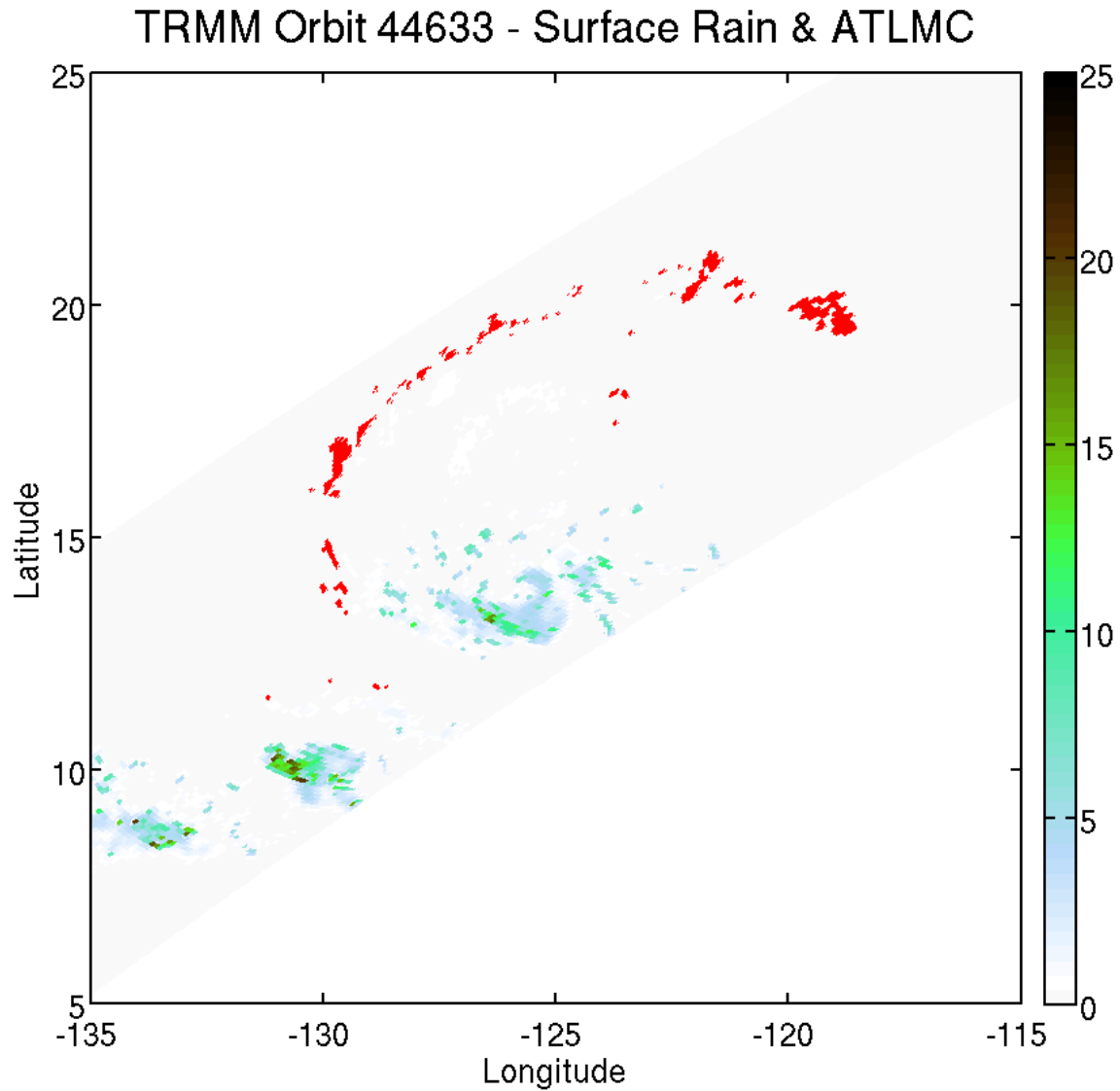
**Figure 2.1.** Average percent low cloud amount based on monthly ISCCP-D2 visible and infrared satellite data from July 1983 through June 2008.



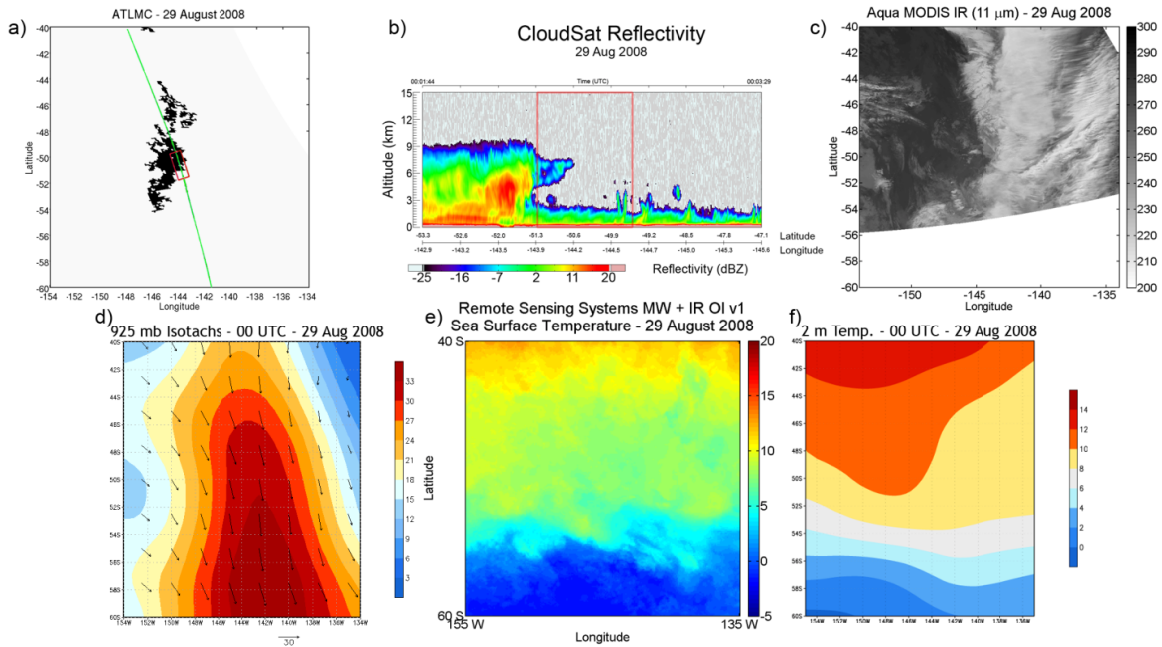
**Figure 2.2.** Matrix of brightness temperature distributions for 60,000 atypically-thick low marine cloud pixels randomly sampled across the TMI domain for 2004. The histograms and scatter density plots show the brightness temperature distributions of atypically-thick low marine cloud for each vertically polarized TMI channel.



**Figure 2.3.** Atypically-thick low marine cloud in the eastern Gulf of Mexico on 5 March 2002. The black area is atypically-thick low marine cloud as flagged by the search algorithm. The blue areas denote cloud that was excluded by the contiguous area filter. The red boundary represents the edges of the atypically-thick low marine cloud and is overlaid over the 10 GHz, 19 GHz, 21 GHz, 37 GHz, and 85 GHz vertically-polarized TMI brightness temperatures.

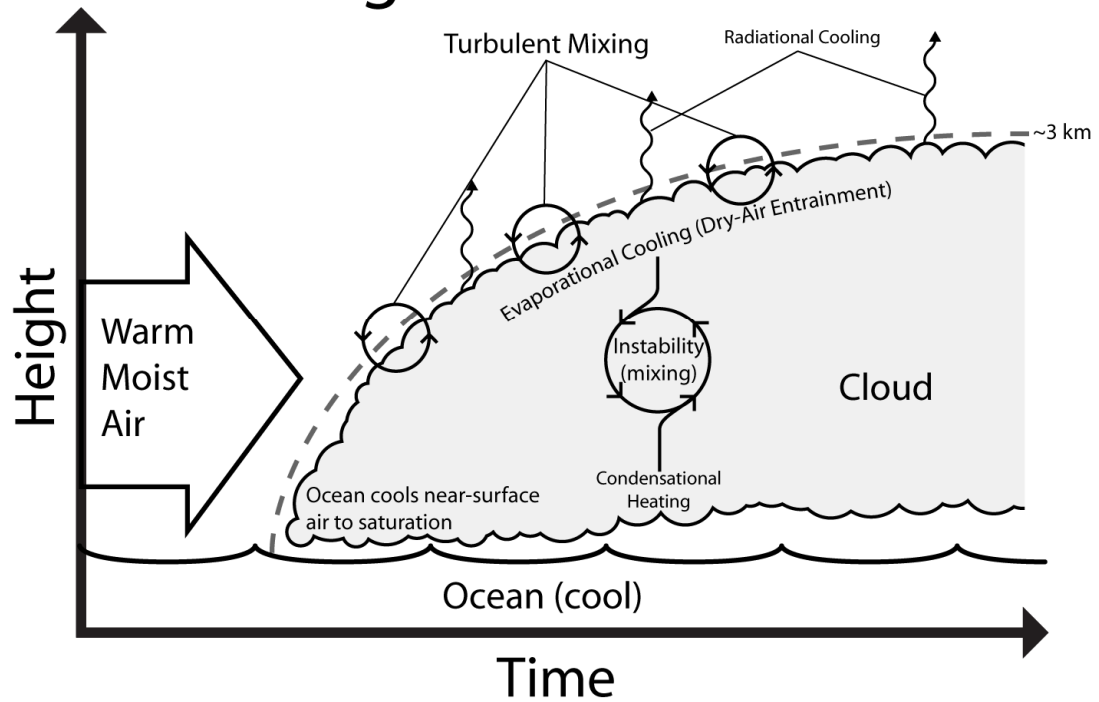


**Figure 2.4.** Algorithm-identified atypically-thick low marine cloud (red) overlaid on TMI near-surface rain rate for TRMM orbit 44633 on 14 September 2005 in the vicinity of Tropical Depression Jove in the eastern Pacific Ocean. The red atypically-thick low marine cloud area is removed since the contiguous areas are less than  $50\ 0.1^\circ \times 0.1^\circ$  pixels.

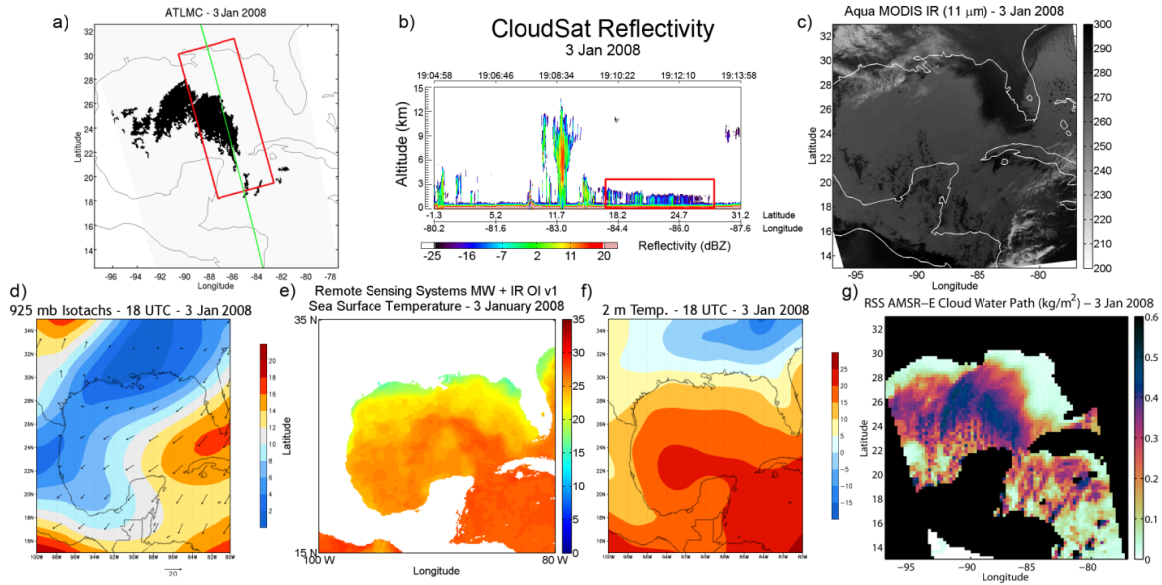


**Figure 2.5.** Atypically-thick low marine cloud (a) and CloudSat reflectivity profile (b) data from 29 August 2008. The green line in panel a) denotes the corresponding CloudSat ground path. The red box in both panels a) and b) highlights the area identified as atypically-thick low marine clouds by the search algorithm. Panel c) is the Aqua MODIS band-31 IR blackbody-equivalent brightness temperatures. Panel d) is the 925 hPa winds from the NCEP/DOE model reanalysis for 18 UTC 29 August 2008. Panel e) is the Remote Sensing Systems Passive Microwave plus Infrared Optimally Interpolated version 1 Sea Surface Temperature for 29 August 2008. Panel f) is the 2 m temperature from the NCEP/DOE model reanalysis for 18 UTC 29 August 2008.

# Advection Fog Genesis

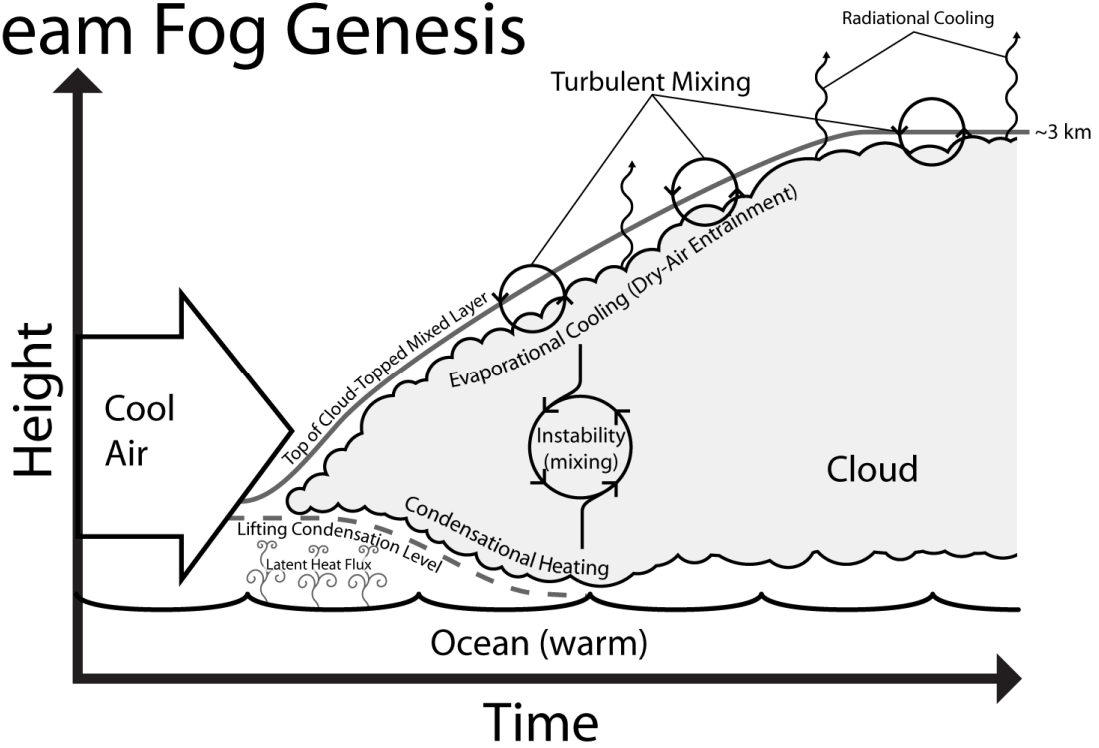


**Figure 2.6.** Schematic of the processes inferred in the transition from advection fog into atypically-thick low marine cloud.



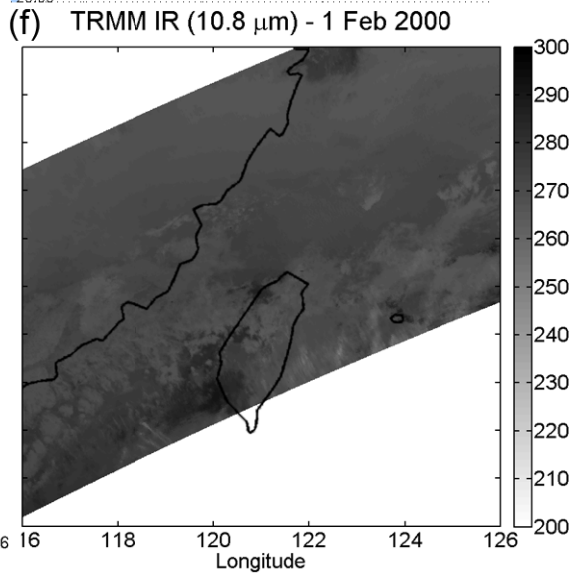
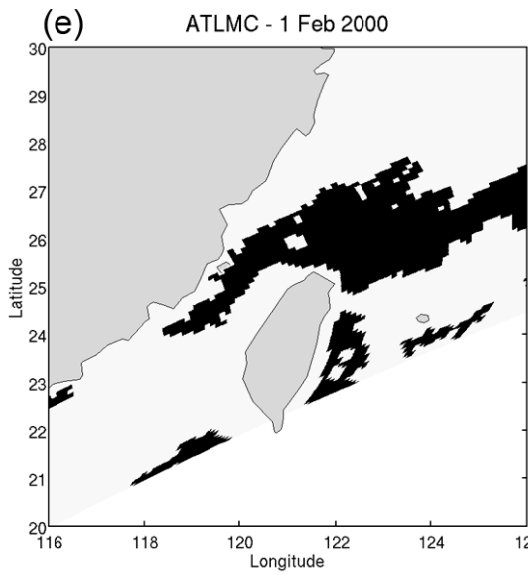
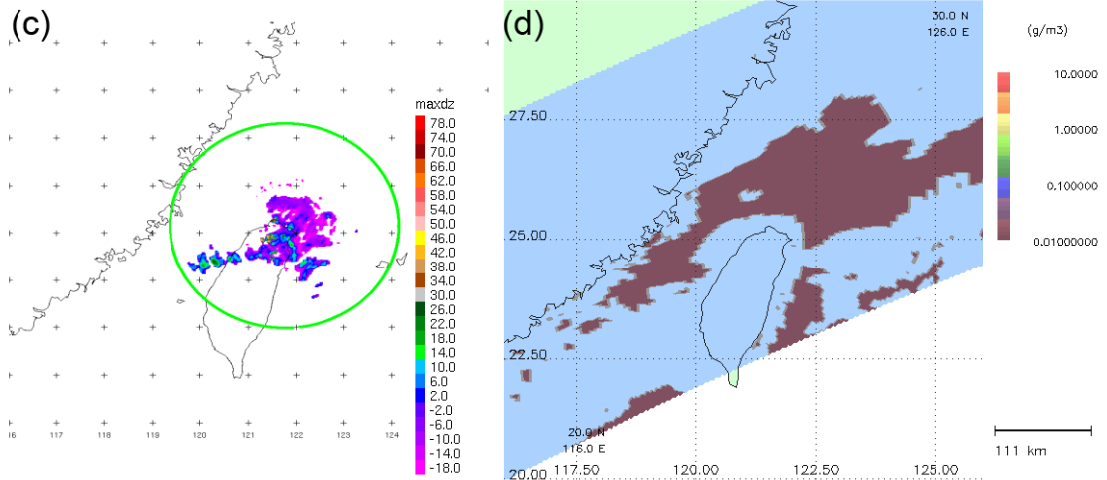
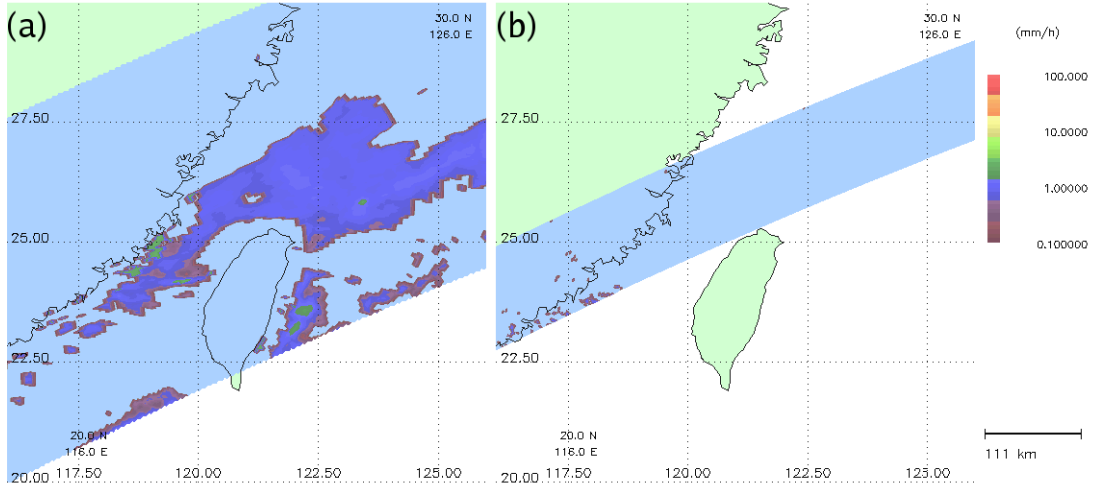
**Figure 2.7.** Atypically-thick low marine cloud (a) and CloudSat reflectivity profile (b) data from 3 January 2008. The green line in panel a) denotes the corresponding CloudSat ground path. The red box in both panels a) and b) highlights the corresponding feature of interest in each panel. Panel c) is the Aqua MODIS band-31 IR blackbody-equivalent brightness temperatures. Panel d) is the 925 hPa winds from the NCEP/DOE model reanalysis for 18 UTC 3 January 2008. Panel e) is the Remote Sensing Systems Passive Microwave plus Infrared Optimally Interpolated version 1 Sea Surface Temperature for 3 January 2008. White denotes land. Panel f) is the 2 m temperature from the NCEP/DOE model reanalysis for 18 UTC 3 January 2008. Panel g) is the Remote Sensing Systems TMI 0.25° cloud water path data for 3 January 2008. Black areas denote either land or missing data.

# Steam Fog Genesis



**Figure 2.8.** Schematic of the processes inferred in the transition from steam fog into atypically-thick low marine cloud.

**Figure 2.9.** Atypically-thick low marine cloud off the Taiwan coast on 1 Feb. 2000. (a) TMI surface precipitation retrieval. (b) PR near surface precipitation. (c) Coastal S-band radar composite. Ring denotes maximum range. (d) 14 km TMI cloud ice above observed cloud top level. (e) Atypically-thick low marine cloud (black). Dark grey denotes land and light grey denotes TMI swath area. (f) TRMM infrared blackbody-equivalent brightness temperatures.



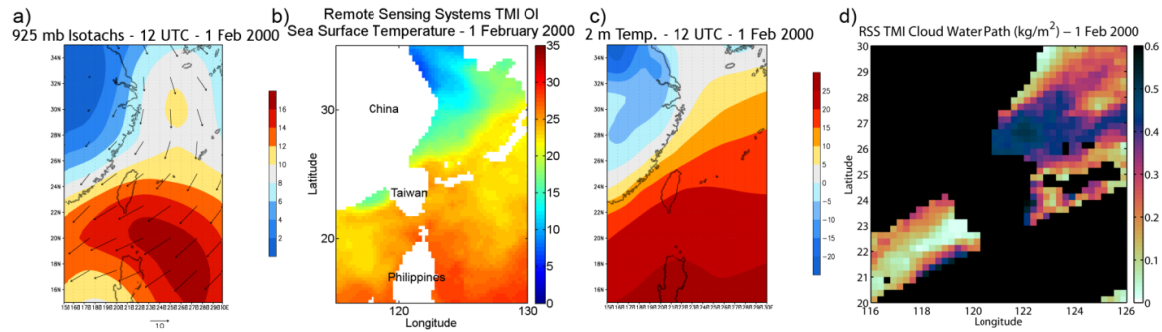


**Figure 2.10.** Additional data sets corresponding to 1 Feb. 2000 case shown in Fig. 2.9. Panel a) is the 925 hPa winds from the NCEP/DOE model reanalysis for 12 UTC 1 February 2000. Panel b) is the Remote Sensing Systems TMI Optimally Interpolated version 1 Sea Surface Temperature for 1 February 2000. The white area denotes land. Panel c) is the 2 m temperature from the NCEP/DOE model reanalysis for 12 UTC 1 February 2000. Panel d) is the Remote Sensing Systems TMI 0.25° cloud water path data for 1 February 2000. Black areas denote either land or missing data.

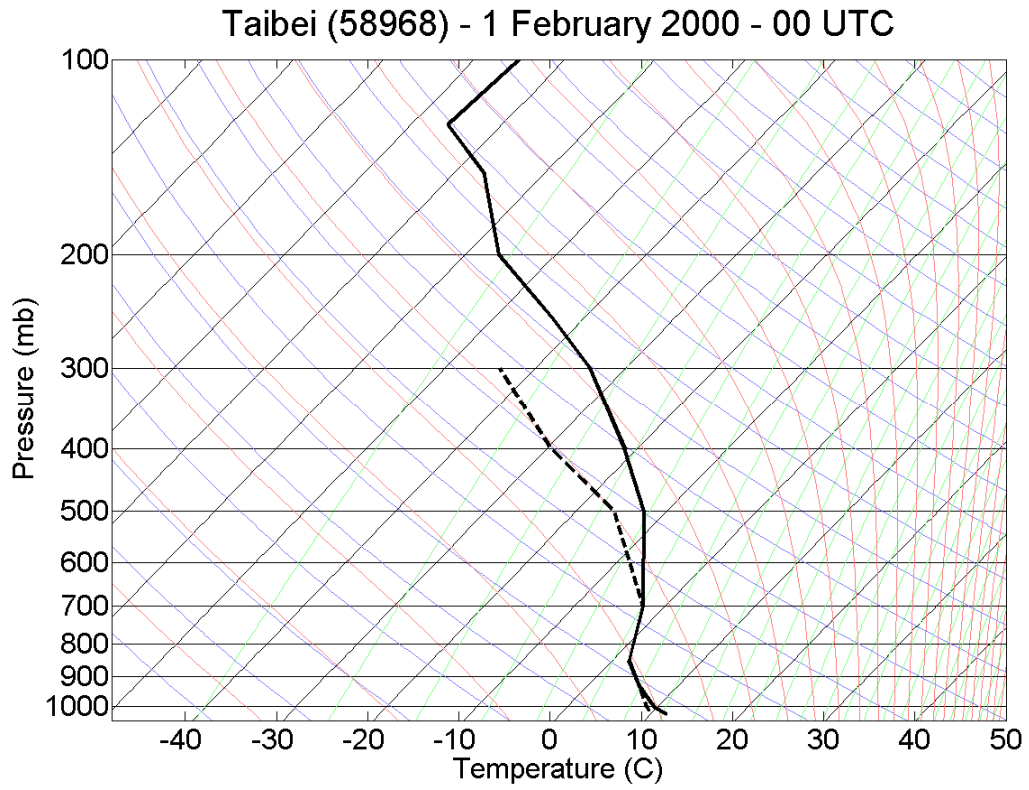


**Figure 2.11.** Skew-T diagram of the 00 UTC sounding from northern Taiwan for 1 Feb. 2000. (Data courtesy of University of Wyoming.)

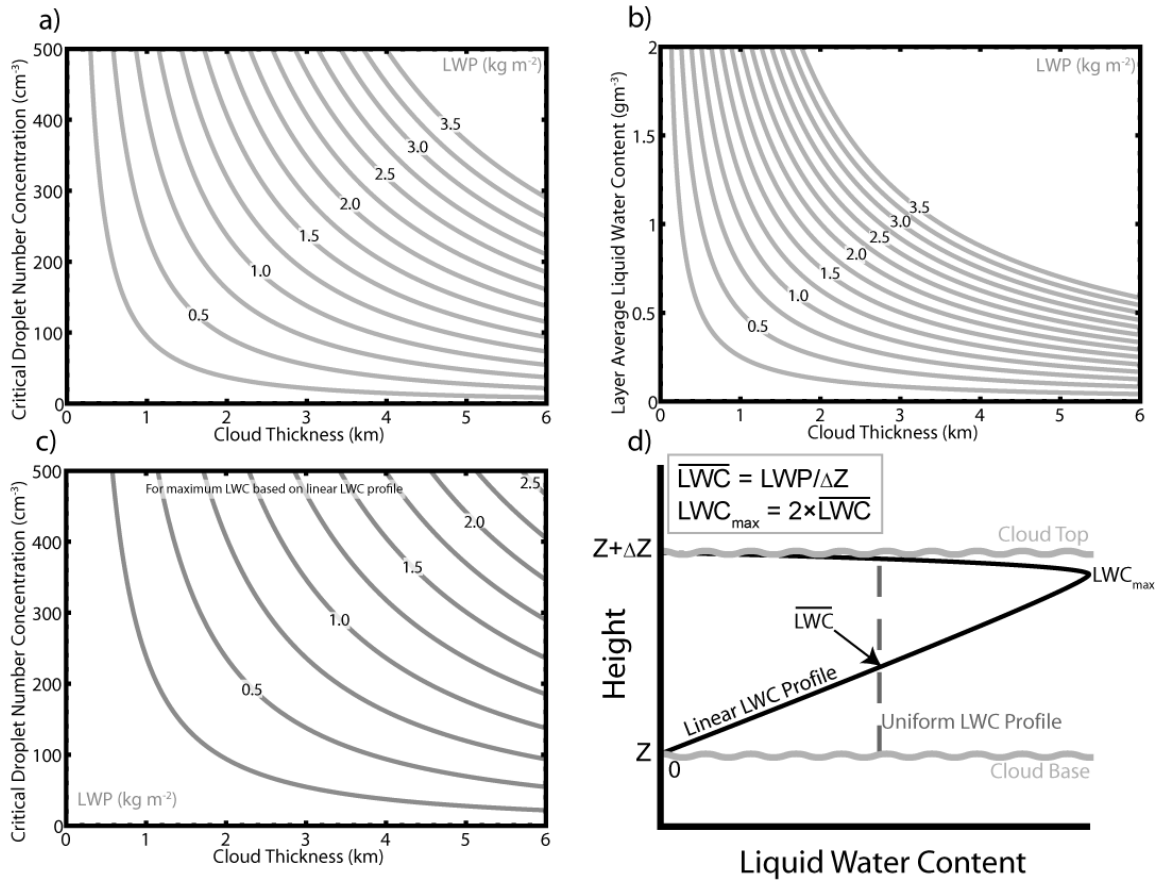


**Figure 2.12.** a) Critical number concentrations for the autoconversion of cloud droplets to precipitation for different LWPs as a function of cloud thickness and droplet number concentration using the Kessler-type parameterization of Liu and Daum [2004] and cloud-average LWC as described by equation (3). For autoconversion from cloud droplets to rain droplet to occur, the number concentration must be less than the critical number concentration. b) Layer Average LWC versus cloud thickness for different LWPs. c) As a) but as a function of maximum LWC and not cloud-average LWC. d) Schematic of the liquid water content profile extremes for atypically-thick low marine clouds: uniform profile (grey dashed line) and a linearly increasing profile (black line).

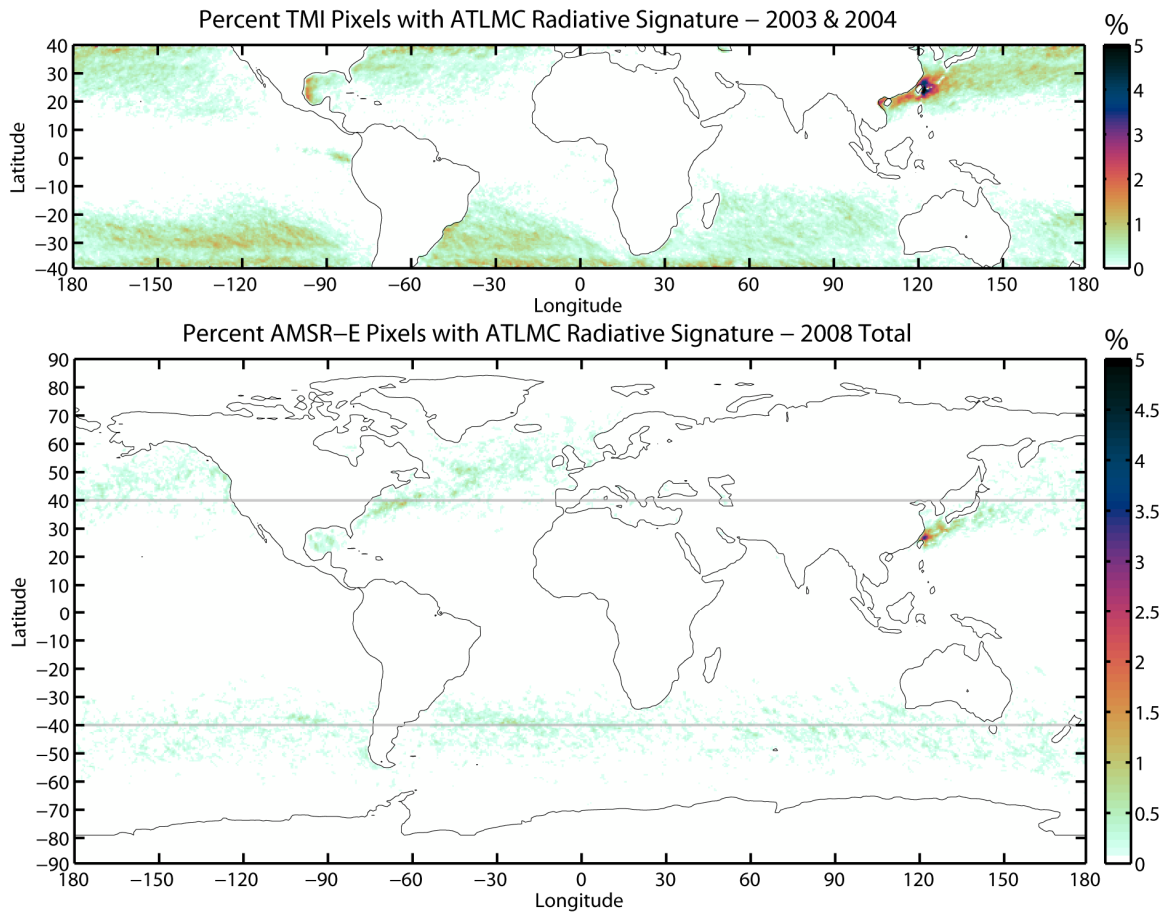


**Figure 2.13.** The percentage of TMI observations with atypically-thick low marine cloud radiative signatures on a  $0.5^\circ$  by  $0.5^\circ$  grid for 2003 and 2004 combined (top) and the percentage of AMSR-E observations with atypically-thick low marine cloud radiative signatures on a  $0.5^\circ$  by  $0.5^\circ$  grid for 2008 (bottom). The horizontal gray lines at  $\pm 40^\circ$  in the bottom panel are a visual guide to show the limits of the TMI-based plots versus the AMSR-E-based plots.

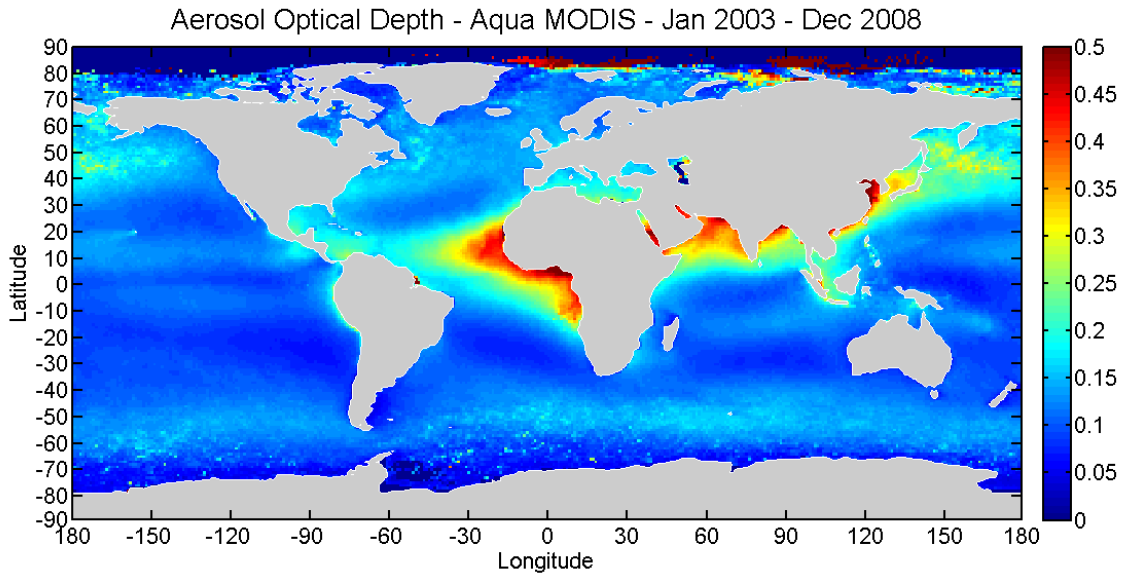


**Figure 2.14.** Average aerosol optical depth at 550 nm based on monthly MODIS-Aqua version 5 data from January 2003 through December 2008. Land areas are masked with the color gray.

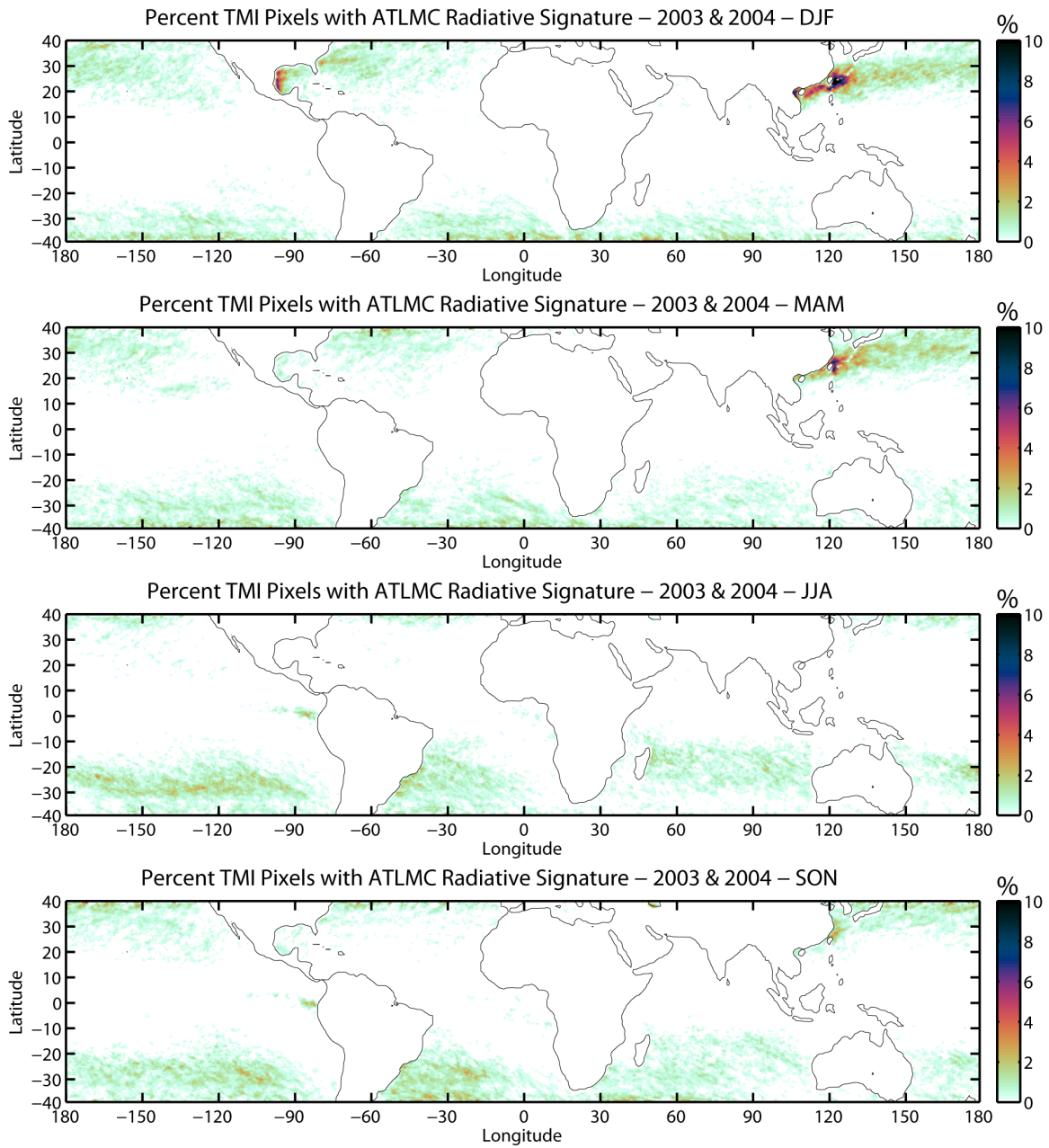


**Figure 2.15.** The percentage of TMI observations with atypically-thick low marine cloud radiative signatures on a 0.5° by 0.5° grid for each season in 2003 and 2004 combined.

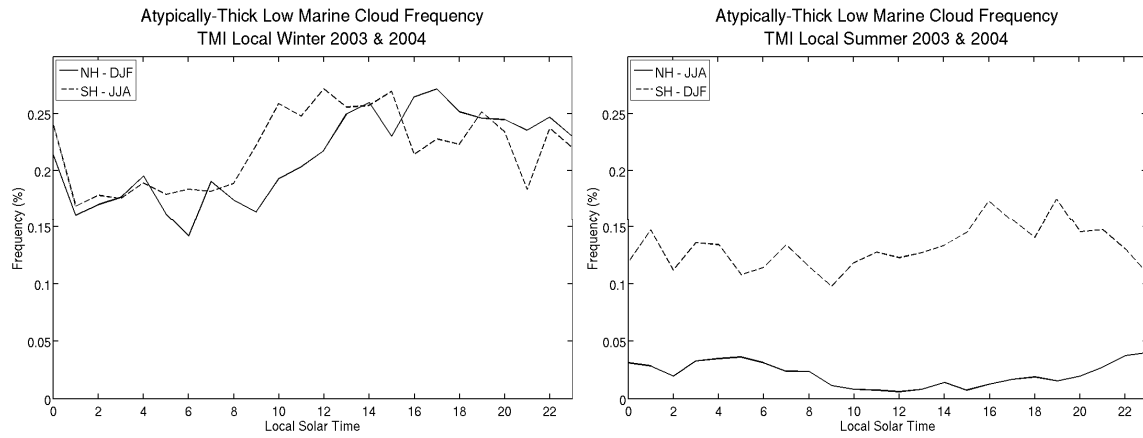


**Figure 2.16.** The frequency of TMI observations flagged as atypically-thick low marine cloud as a function of LST, latitude, season, and hemisphere for TMI observations from 2003 and 2004 combined. Local hemisphere winter and summer are represented in the left-hand and right-hand panels respectively (December, January, and February (DJF); June, July, and August (JJA)).

# **Chapter III - The Feasibility of Satellite 89 GHz Passive Microwave Measurements for the Detection and Characterization of Drizzling Marine Stratocumulus**

## **3.1. Introduction**

Marine stratocumulus clouds cover vast regions of the eastern subtropical oceans and play a significant role in moderating the climate. Figure 2.1 shows five large areas of low clouds, predominately comprised of marine stratocumulus, off the western coasts on continents in the subtropics. These low, persistent, liquid-phase clouds exert a net cooling effect by reflecting large quantities of incoming solar radiation back into space. The large spatial extent and high albedo of these cloud decks contribute to their significant cooling effect in the earth's radiation budget [Hartmann et al., 1992]. Despite their recognized importance, the radiative properties of marine stratocumulus remain poorly simulated in global circulation models and constitute a major source of uncertainty in climate simulations [Bony et al., 2006]. Numerous studies have documented the deficiencies of general circulation models at simulating the structure of these cloud-topped boundary layers [Bony and Dufresne, 2005; Cronin et al., 2006; Wyant et al., 2006; Wyant et al., 2009]. Much of the uncertainty arises from sub-grid scale variability in the cloud albedo that is not accurately parameterized in climate models [George and Wood, 2009].

For the purpose of climate change simulations, it is not sufficient for coupled general circulation models to model the mean state characteristics. Cloud feedbacks must also be

modeled correctly so that the model components respond to variability and climate change appropriately. Radiative characteristics of marine stratocumulus are closely tied to cloud fraction. Cloud albedo differs dramatically between regions of continuous unbroken cloud versus regions with mesoscale pockets of open cells [Stevens et al., 2005]. Observational and modeling studies have implicated drizzle in the formation of pockets of open cells within the closed cell cloud deck [Stevens et al., 2005; van Zanten and Stevens, 2005; Comstock et al., 2007; Savic-Jovic and Stevens, 2008; Wang and Feingold, 2009]. These studies and more recent observations suggest that drizzle is a necessary but not sufficient condition for the formation of pockets of open cells. The spatial and temporal distributions of drizzle within marine stratocumulus clouds are hence key parameters of interest. For the purposes of this paper, we focus on more intense drizzle cells with radar reflectivity  $> 0$  dBZ and liquid water path (LWP)  $\geq 200$  g/m<sup>2</sup> corresponding to the subset of drizzle features within marine stratocumulus with sufficiently heavy drizzle that precipitation reaches the surface. It is the heavier drizzle cells that are implicated in transitions between closed and open cellular mesoscale cloud structures [Stevens et al., 2005; Comstock et al., 2007; Wood et al., 2010].

The goal of this study is to demonstrate the feasibility of using 89 GHz AMSR-E passive microwave brightness temperature data to detect drizzling marine stratocumulus. A drizzle-proxy product is described that can be used to determine areal and feature statistics of drizzle cells within the major marine stratocumulus regions. The multi-year (since 2002) AMSR-E data set [Kawanishi et al., 2003] is now sufficiently large to

provide an opportunity to examine the regional drizzle precipitation climatology in the context of inter-annual variability.

A new method to document drizzle cell occurrence within marine stratocumulus clouds is needed to supplement existing observations, each of which has limitations. The key limitation of the MODIS Cloud Water Path product for the detection of drizzle cells is that it is not available at night. While drizzle does occur in marine stratocumulus regions during daylight hours, more frequent and intense marine stratocumulus drizzle typically occurs at night when LWP values are higher [Bretherton et al., 2004, Comstock et al., 2005; Sharon et al., 2006]. Any method attempting to ascertain the regional characteristics of drizzle while excluding nighttime drizzle would miss the mode of the drizzle cell distribution and hence would not produce a robust representation of regional drizzle characteristics. Current passive microwave LWP products [Wentz and Meisner, 2000; Kida et al., 2009] are at too coarse a spatial resolution to adequately resolve small and intense drizzle cells which are typically 1-10 km in horizontal dimension. 89 GHz passive microwave brightness temperature data are available at resolutions fine enough to detect individual drizzle cells. The CloudSat radar [Stephens et al., 2002; Haynes and Stephens, 2007; Stephens et al., 2008] has a minimum sensitivity of -28 dBZ and provides information on the vertical structure (x-z) of clouds. For observing marine stratocumulus, cloud top heights and the profile of reflectivity are important physical constraints for column-integrated passive microwave data. However, CloudSat's swath width of 1.4 km is not adequate to obtain information on the horizontal (x-y) mesoscale organization of drizzle. The Tropical Rainfall Measuring Mission Satellite's Precipitation

Radar, with its minimum sensitivity of  $\sim 18$  dBZ, can only detect the subset of the very strongest drizzle cells, so it is not suitable for observing marine stratocumulus

[Kummerow et al. 1998].

### **3.2. Methodology**

Work with ground-based upward-looking radiometers has shown a strong response of 90 GHz to cloud liquid water [Crewell and Löhnert, 2003]. In the absence of ice, satellite downward-looking 89 GHz brightness temperatures are the net result of column-integrated emission and scattering of upwelling radiation by the ocean-surface, water vapor, and liquid hydrometeors which in turn are primarily a function of the background ocean-surface emission (primarily related to SST and wind speed), the gas absorption model, the water vapor profile, cloud-fraction/beam-filling, and the liquid water path (including cloud and precipitable water) [Westwater et al., 2001; Crewell and Löhnert, 2003; Horváth and Gentemann, 2007; Greenwald et al. 2007; Greenwald, 2009]. Of these, we expect that precipitation LWP will have the largest variance at spatial scales  $< 50$  km within marine stratocumulus. Based on multiple years of ship and buoy data for the southeast Pacific marine stratocumulus region, SST typically varies between  $16^\circ$  C to  $20^\circ$  C and near-surface winds are usually  $< 10$  m s<sup>-1</sup> [Bretherton et al., 2004; Comstock et al., 2007]. The typical increase in ocean brightness temperature as a function of wind speed is 1 K per m s<sup>-1</sup> [Petty, 2006].

### **3.2.1 Background Emissitivity**

SST and near-surface wind speed data were examined in relation to 89 GHz AMSR-E brightness temperature data for clear-sky instances. For a quantitative estimate of LWP, SST and wind data need to tightly constrain a value of background 89 GHz brightness temperature for use as a reference in determining the magnitude of the brightness temperature maxima created by drizzle cells. As is illustrated in Figure 3.1, there is a wide spread of brightness temperature values for any given SST, particularly for SSTs between 20° C and 30° C. Wind speed alone is not enough to account for this variability. This wide joint-variability of SST, near-surface wind, and 89 GHz brightness temperature for cloud-free pixels means that there is insufficient information in pixels with clouds to constrain a quantitative estimate of LWP based on a combination of these three variables. One possible source of variability is column-integrated water vapor. It may also be possible that different combinations of SST, wind, and LWP can have the same brightness temperature value. Our method of identifying drizzle cells focuses on local maxima in 89 GHz brightness temperature (i.e. spatial feature detection) rather than absolute thresholds.

### **3.2.2 Identification of Drizzle Cells**

Areas of high liquid water path related to drizzling cloud appear as local maxima in the AMSR-E 89 GHz brightness temperature data when no ice is present. Inversion-topped boundary layers in the subtropical regions constrain marine stratocumulus cloud tops to well below the 0°C level, precluding the existence of ice and making these clouds a prime

candidate for the exploitation of 89 GHz data for a high resolution drizzle identification technique. Figure 3.2 illustrates the advantage of the higher spatial resolution AMSR-E Level 2 89 GHz brightness temperatures ( $6 \times 4$  km) compared to AMSR-E Level 2 Liquid Water Path (12 km resolution) which is based primarily on 37 GHz brightness temperatures ( $10 \times 14$  km) [Wentz and Meissner, 2000, 2004]. Areas of drizzle detected by the NOAA Ship Ronald H. Brown C-band radar (minimum detection threshold  $\sim 0$  dBZ) are closely aligned with clumps of higher brightness temperature observed by AMSR-E 89 GHz. These drizzle cells are present in the AMSR-E Liquid Water Path product but are less well resolved. The MODIS Cloud Water Path data, which are based on 1 km VIS/IR data, most closely corresponds to the 500 m resolution C-band radar data.

We sidestep the complexities of quantitative LWP retrieval by calculating a drizzle-proxy based on the brightness temperature difference ( $\Delta T_b$ ) between the drizzling cloud and its non-drizzling surroundings. We utilize satellite-derived SST and wind products [Donlon et al., 2002] in conjunction with AMSR-E brightness temperatures for available cloud-free pixels to estimate  $\sim 50$  km scale variations in background emissivity. Based on the ship C-band radar data from the EPIC Sc and VOCALS cruises, drizzle cells  $> 0$  dBZ tend to have sharp gradients in LWP which will aid in their identification. The horizontally polarized 89 GHz brightness temperature channel is used in this study because it contains less noise than the vertically-polarized channel.

Based on iterative refinement, the follow steps were used to identify drizzle cells in 89 GHz brightness temperature data:

For each pixel:

Is  $283 \text{ K} \leq \text{SST} \leq 298 \text{ K}$ ?

If yes, is Cloud Top Temperature  $> 273 \text{ K}$ ?

If yes, is  $\text{Tb}_{89\text{H}} - \text{SST} \geq \Delta\text{Tb}$

If yes, flag pixel as likely drizzle

On binary array with pixels flagged as likely drizzle:

Identify contiguous areas

$\text{Tb}_{89\text{H}}$  is the AMSR-E horizontally polarized 89 GHz brightness temperature in Kelvin, SST is the AMSR-E sea surface temperature estimate in Kelvin (AMSR-E L2\_Ocean product), and  $\Delta\text{Tb}$  a threshold value set by the user. Cloud top temperature was taken from the gridded MYD08\_D3 daily MODIS product. This simple method for defining drizzle was shown to perform just as well as methods based on multiple regression techniques or methods using morphological operations to identify local maxima. As the scatter density plots in Figure 3.1 illustrate, sea surface temperature and winds do not account for all the variation in clear-sky 89 GHz brightness temperatures so using a multiple regression method to define drizzle is of limited utility in this circumstance. Based on several case studies examined, the optimal value of  $\Delta\text{Tb}$  varies slightly among geographic regions. For the SE Pacific and SE Atlantic,  $\Delta\text{Tb}=-45.4 \text{ K}$  works well, but a higher value was needed for the NE Pacific. These drizzle detection criteria perform

reasonably well, but they are offered here with the understanding that they may be refined with future research.

The identification of discrete contiguous areas is done using a “blob” detection technique based on standard algorithms used to identify contiguous 4-connected or 8-connected groups of pixels in raster data where pixel groups can be defined based on any query returning a binary result [Rosenfeld and Pfaltz, 1966; Haralock and Shapiro, 1992].

Figure 3.3 is a schematic illustrating the difference between 4 and 8 pixel connectivity. Once the discrete drizzle cells are identified using a blob detection algorithm, various statistics can be calculated including, but not limited to: cell area, aspect ratio, and orientation as well as frequency of occurrence per unit area.

### **3.3. Stratocumulus Detection Examples**

#### **3.3.1 Southeast Pacific**

Figure 3.4 shows co-registered 89 GHz brightness temperature data, AMSR-E and MODIS LWP data, the detected drizzle field, and the MODIS visible imagery for an area over the southeast Pacific on 27 October 2008. As was illustrated in Figure 3.2, areas of higher LWP have corresponding higher 89 GHz brightness temperatures. The sea surface temperatures for this area were used to calculate a background temperature value.

Comparison of the 89 GHz based drizzle product to a field of AMSR-E LWP values  $\geq 200 \text{ g/m}^2$  shows that 89 GHz is able to identify more small areas of drizzle. The value of  $200 \text{ g/m}^2$  was chosen as the threshold for drizzle in the AMSR-E LWP product after

comparing the LWP data to the radar data in Figure 3.2. The absence of smaller drizzle cells in the AMSR-E LWP product is primarily due to the more coarse spatial resolution of the AMSR-E LWP product. The small drizzle features in the 89 GHz based product correspond well to the small areas of high LWP values in the MODIS LWP product.

Figure 3.5 contains histograms of area for discrete drizzle cells for the example scene from the southeast Pacific in Figure 3.4. Discrete drizzle areas were identified using both 4-connected and 8-connected techniques. The majority of the drizzle cells have areas less than five  $6 \times 4$  km 89 GHz pixels. In comparing the histograms for the 89 GHz versus the AMSR-E LWP based drizzle products, the 89 GHz based product is more granular with respect to detecting small drizzle cells. This highlights one of the key reasons to use an 89 GHz based drizzle product over the existing AMSR-E LWP product. Since the majority of drizzle areas are small, the 89 GHz based product is better suited to detecting differences and changes in the frequency of small drizzle cells.

8-connected contiguous area algorithms inherently produce fewer, larger discrete groups since there are more ways for pixels to be connected to each other as opposed to a 4-connected technique. This can readily be seen in Figure 3.5 when comparing the left-hand 4-connected data to the right-hand 8-connected data. For the 8-connected data, there are fewer and larger drizzle cells as compared to the 4-connected data for either the 89 GHz or the AMSR-E LWP based drizzle products. The choice of 4-connectivity or 8-connectivity does not produce any obvious differences in the shapes on the area

distributions for this scene. The differences between 4-connected and 8-connected contiguous feature techniques decreased as the mode of the feature's areas increased.

### **3.3.2 Southeast Atlantic**

Satellite data from a scene with drizzle over the southeast Atlantic off the coast of Africa for 26 June 2007 are shown in Fig. 3.6. The marine stratocumulus common to this region have never been the subject of a major field observation campaign. Areas with high LWP values stand out as local maxima in 89 GHz brightness temperature data. The 89 GHz and AMSR-E LWP based drizzle products both detect drizzle in the same general areas. The 89 GHz based product includes small drizzle cells that are absent from the AMSR-E LWP based product. Comparison of the drizzle fields to the MODIS LWP field shows that the smaller drizzle areas of the 89 GHz product correspond better to the high resolution LWP information. There are some high, mostly transparent, cirrus clouds in this scene with cloud top temperatures below the criteria for drizzle detection. These clouds account for the differences in drizzle detection between the 89 GHz and AMSR-E LWP based products in the  $-17^\circ$  latitude band.

### **3.3.3 Northeast Pacific**

Satellite data for an area over the northeast Pacific for 29 July 2009 that contains drizzle is shown in Fig. 3.7. This area is an example of a situation where different regions or circumstances may require different drizzle detection criteria. In this case,  $\Delta T_b = -38$  K was used since  $\Delta T_b = -45.4$  K did not reproduce the cellular pattern of LWP in the AMSR-E or MODIS products. The drizzle areas in the 89 GHz products are larger than

the AMSR-E based areas, contrary to the previous examples. High sea surface temperature values are a possible source of error in this case. 89 GHz brightness temperatures are much higher in the southern half of this scene as compared to the other examples. This scene indicates that the method needs further refinement. One possible avenue is the use of MODIS LWP scenes in the few days before and after to tune the 89 GHz  $\Delta T_b$  value and will be explored in future work.

### **3.4. Conclusions**

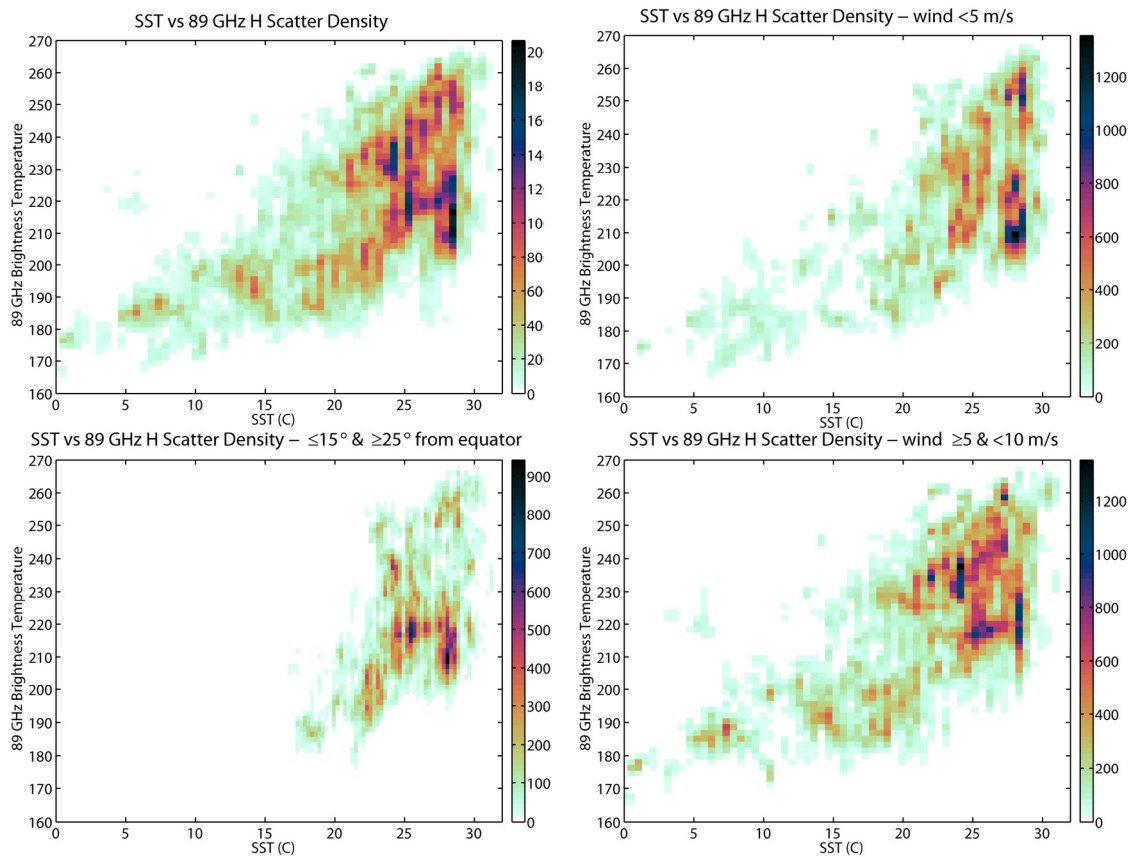
Drizzle has been identified as playing a key role in the evolution of marine stratocumulus and the transitions between closed and open cellular states. To better understand these transitions and the role drizzle plays, a routine method of detecting drizzle cells is needed. Satellite-based observation is well suited to the remote location of typical marine stratocumulus areas. However, current satellite methods are either lacking in resolution or diurnal coverage. Using high-frequency passive microwave observations to detect drizzle in marine stratocumulus allows for consistent observations at resolutions sufficient for resolving individual heavy drizzle cells. Future work is planned for extending this methodology to the TRMM microwave radiometer 85.5 GHz channel in order to provide diurnal coverage the AMSR-E cannot.

Emission by precipitation liquid water from drizzle cells in marine stratocumulus regions yields local maxima in brightness temperature in 89 GHz data. SST data can be used to help constrain a background brightness temperature value to which these local maxima

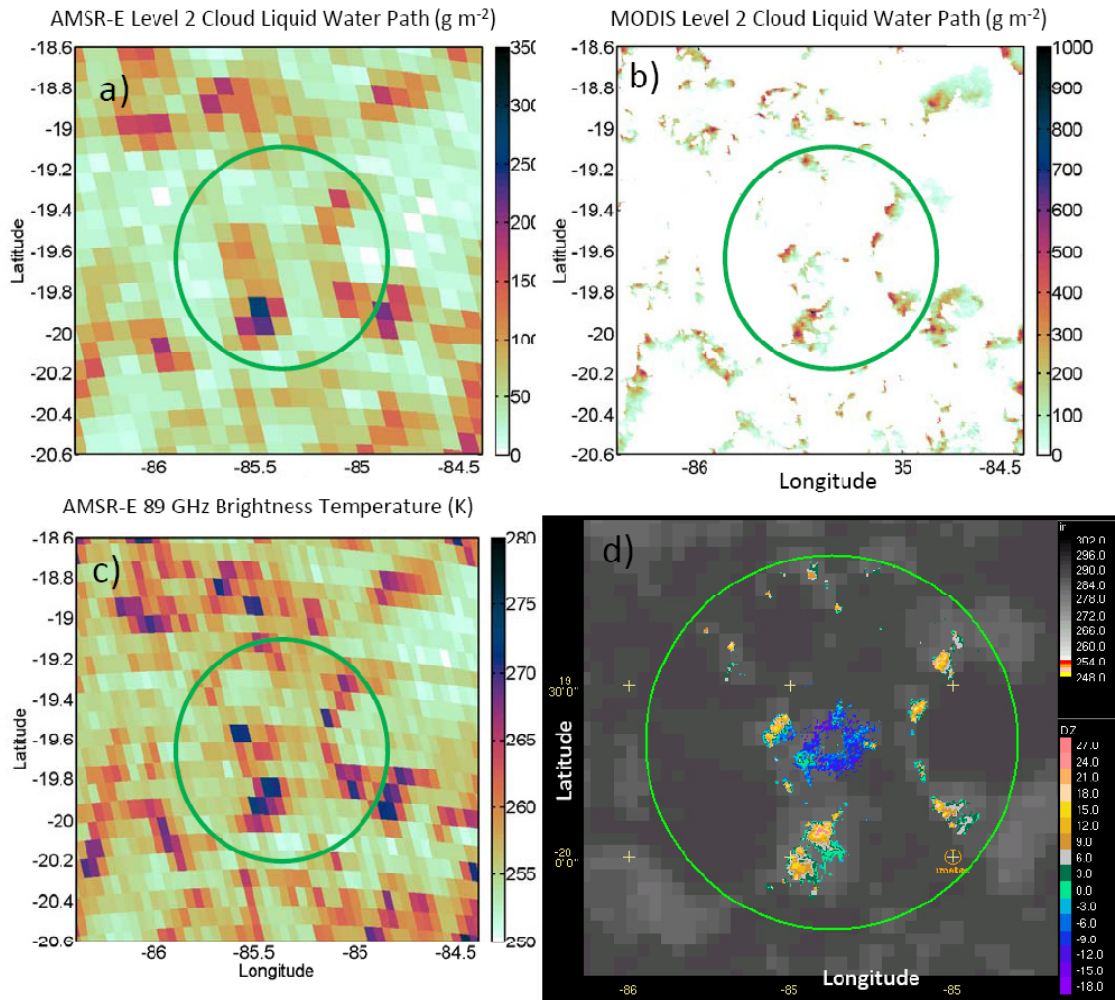
can be compared. Once drizzle is identified, “blob” detection algorithms are used to identify discrete drizzle cells and calculate various spatial statistics.

Even without an accompanying quantitative estimate of drizzle LWP, the identification of drizzle cells within marine stratocumulus regions with satellite data will permit analysis of seasonal and regional drizzle cell occurrence. The characteristics of contiguous drizzle cell features can be documented: the number of drizzle cells per unit area, their sizes and shape, and the distances between cells. These properties in turn can be used as comparison metrics among the marine stratocumulus regions and will provide an avenue for evaluation of numerical model parameterizations. Use of the AMSR-E 89 GHz 6 km  $\times$  4 km brightness temperatures reduces beam-filling errors compared to current AMSR-E LWP products. The drizzle proxy product based on satellite 89 GHz information represents a new approach using downward-looking passive microwave data that provides information on the frequency of occurrence and spatial characteristics of drizzle with the aim of better understanding the role of drizzle in the evolution of marine stratocumulus.

## Chapter III - FIGURES

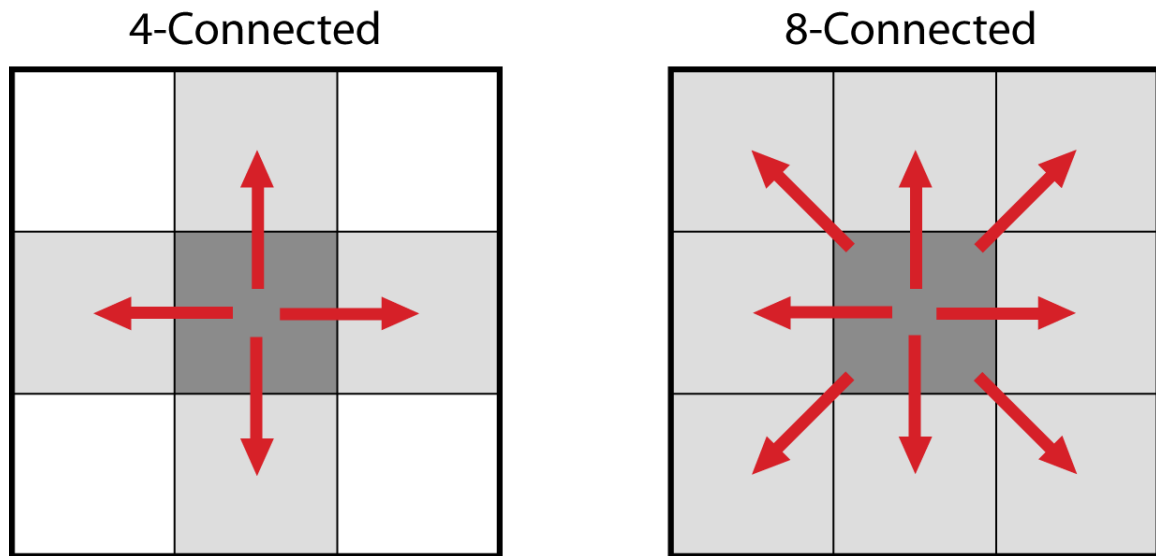


**Figure 3.1.** Scatter density plot of clear-sky SST versus Level 2 AMSR-E 89 GHz horizontally polarized brightness temperatures. Clear sky determination is based on 1 degree resolution level 3 Aqua MODIS cloud fraction data where values are less than 1%. Each AMSR-E 89 GHz pixel was assigned a cloud fraction value based on the value of the nearest MODIS cloud fraction pixel. SST values were derived from Remote Sensing Systems 0.25 degree Version-5 AMSR-E Ocean Product. Each AMSR-E 89 GHz pixel was assigned a SST value based on the value of the nearest Remote Sensing Systems SST pixel. The color scale represents the pixel count per bin in all cases.



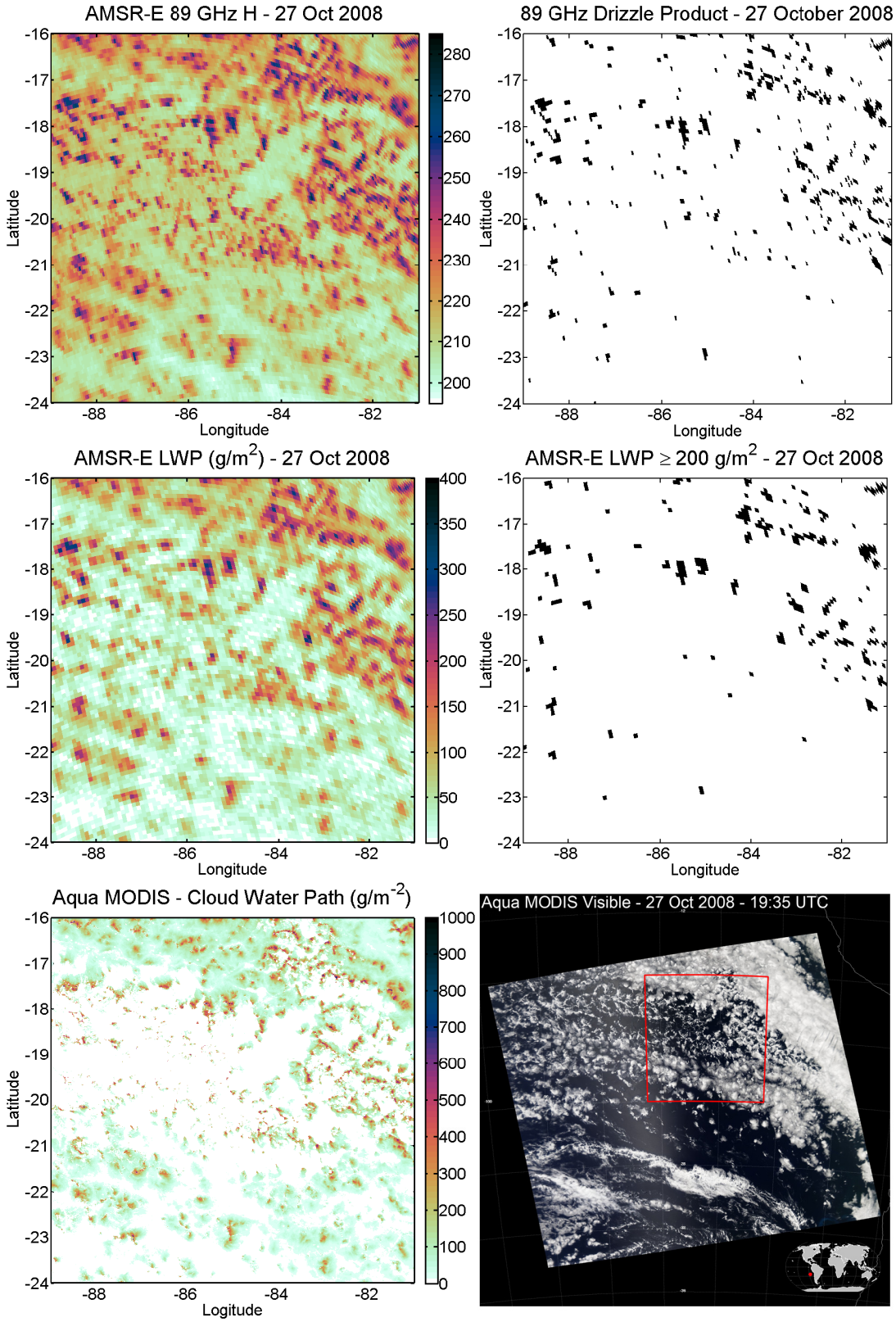
**Figure 3.2.** Detailed comparison among a) AMSR-E Level 2 Liquid Water Path, b) MODIS Level 2 Cloud Water Path, c) AMSR-E Level 2 89 GHz brightness temperature and d) C-band ship-borne radar data obtained at 1936 UTC on 27 October 2008 in the SE Pacific during VOCALS experiment. The 60 km radius range ring from the radar is overlaid on each image. In order to highlight gradients in LWP, the dynamic range of the color scales differ between a) and b).

# Pixel Connectivity



**Figure 3.3.** Schematic illustrating the difference between 4 and 8 pixels connectivity. 4-Connected pixels are considered adjacent if they share one their four sides. 8-Connected pixels are considered adjacent if they share a side or a diagonal.

**Figure 3.4.** Drizzle information for the southeast Pacific on 27 October 2008 at  $\approx$ 19:35 UTC. The upper-left panel in AMSR-E horizontally polarized 89 GHz brightness temperature from the L2A product. The middle-left panel is AMSR-E liquid water path from the L2\_Ocean product. The lower-left panel in the Aqua MODIS daytime mean cloud water path from the MYD06\_L2 product. The upper-right panel in the 89 GHz based drizzle detection. The black areas denote drizzle. The middle-right panel is the AMSR-E LWP based drizzle product where drizzle is any area with  $LWP \geq 200$  g/m<sup>2</sup>. The black areas denote drizzle. The bottom-right panel in the Aqua MODIS visible imagery quick-look image ([http://modis-atmos.gsfc.nasa.gov/IMAGES/index\\_myd021km.html](http://modis-atmos.gsfc.nasa.gov/IMAGES/index_myd021km.html)).



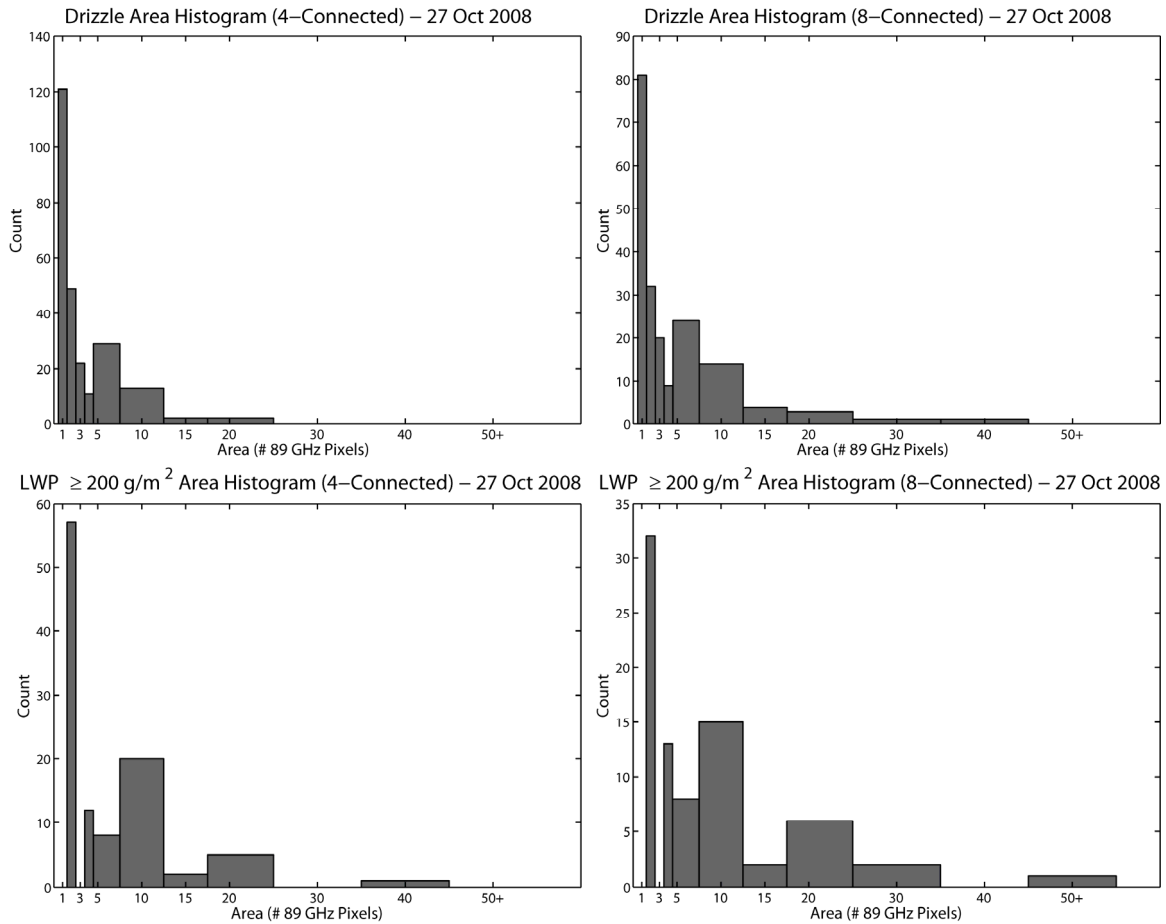


**Figure 3.5.** Histograms comparing drizzle area based on 89 GHz drizzle proxy versus AMSR-E LWP for the region show in Figure 3.4. All areas are in units of number of 89 GHz pixels ( $6 \text{ km} \times 4 \text{ km}$ ). The upper-left panel is the area histogram for 4-connected contiguous drizzle pockets detected using 89 GHz brightness temperature data. The upper-right panel is the area histogram for 8-connected contiguous drizzle pockets detected using 89 GHz brightness temperature data. The lower-left panel is the area histogram for 4-connected contiguous drizzle pockets defined as contiguous areas with AMSR-E LWP  $\geq 200 \text{ g/m}^2$ . The lower-right panel is the area histogram for 8-connected contiguous defined as contiguous areas with AMSR-E LWP  $\geq 200 \text{ g/m}$ .

**Figure 3.6.** As Figure 3.4 but for the southeast Atlantic on 26 June 2007 at  $\approx 13:05$  UTC.

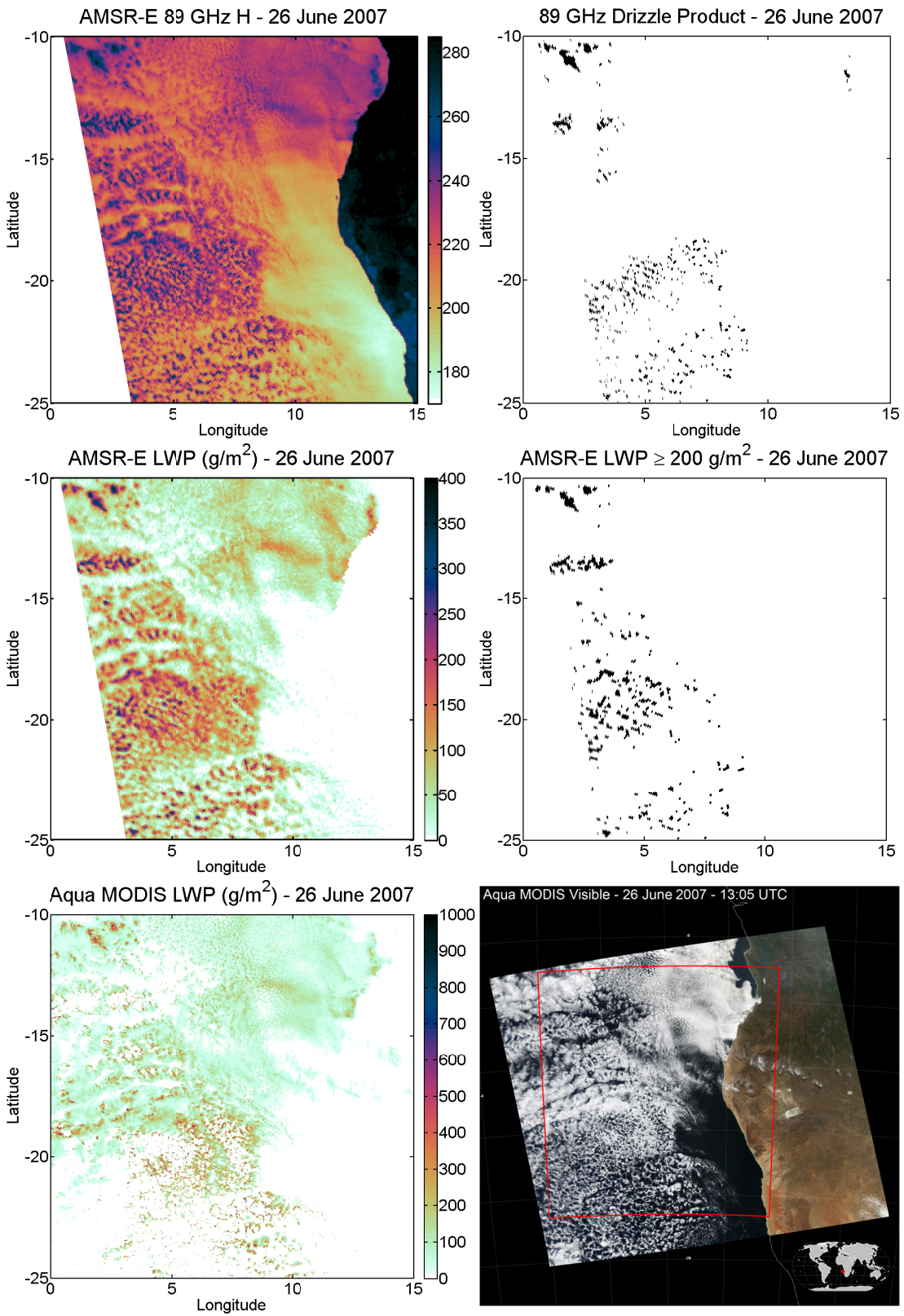
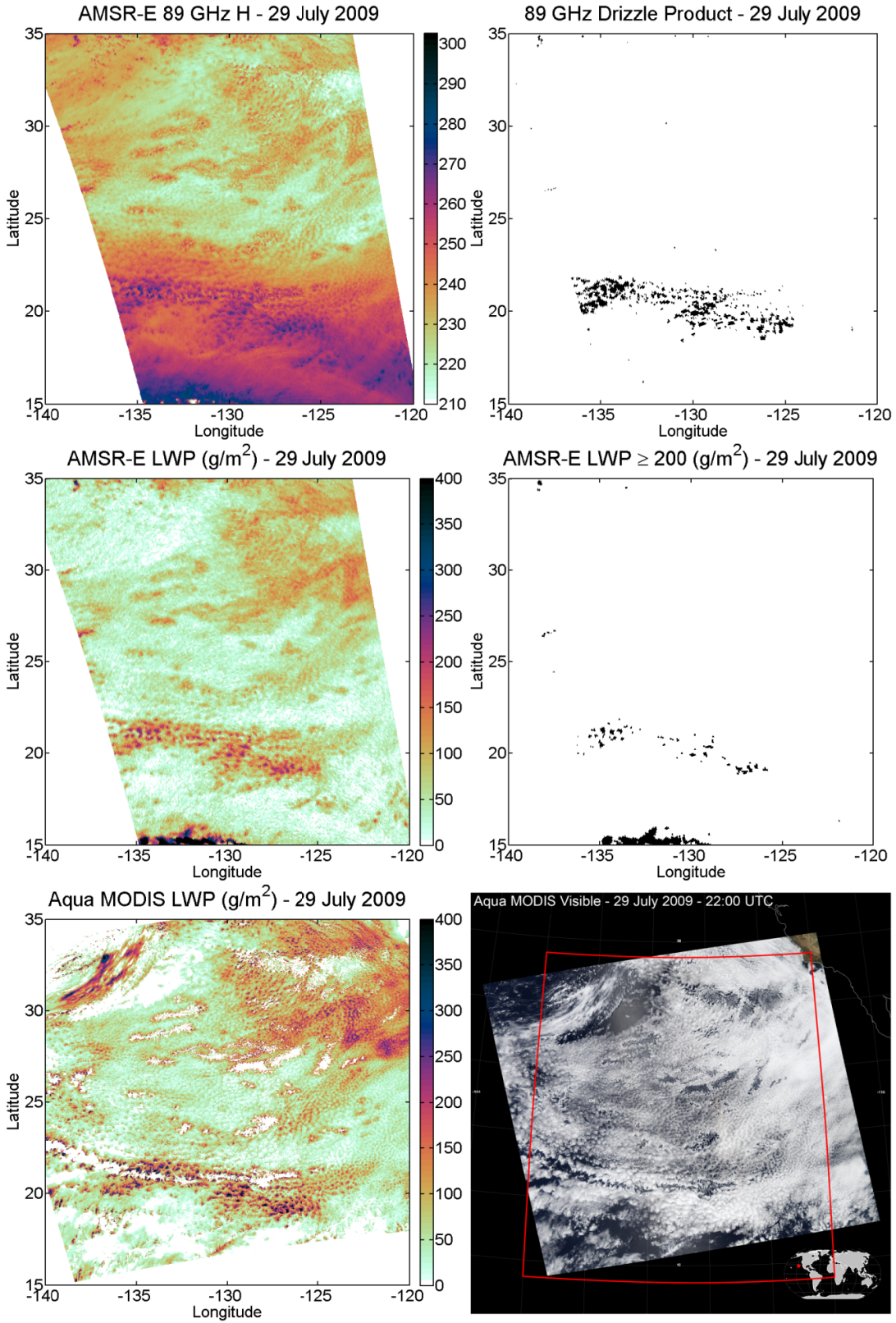


**Figure 3.7.** As Figure 3.4 but for the northeast Pacific on 29 July 2009 at  $\approx 22:00$  UTC.



## **Chapter IV - Future Work**

### **4.1 Atypically Thick Low Marine Clouds**

Chapter II used passive microwave data for the identification of atypically-thick low marine clouds. The spatial and temporal frequencies of their occurrence were examined. Data from other sensors complemented the climatologies by providing physical details of their structure and genesis. However, there remains much work before a detailed understanding of atypically-thick low marine clouds and their overall significance is attained.

#### **4.1.1 Quantifying Passive Microwave Precipitation Bias**

One of the characteristics of atypically-thick low marine clouds is that they do not rain above the TRMM PR detection threshold of 0.4 mm/hr. However, atypically-thick low marine clouds are erroneously indicated as raining with modal values of 0.6 to 1.2 mm/hr in passive microwave products based on the Goddard Profiling Algorithm. Such products include TRMM's TMI based 2A12 precipitation product and AMSR-E's precipitation products. The rainfall bias in these passive microwave rainfall products, resulting from the false-positive rainfall indication induced by atypically-thick marine clouds, can be computed using data from the atypically-thick marine cloud search algorithm. By subtracting any atypically-thick low marine cloud pixels that are also raining pixels from passive microwave rainfall products, the bias induced by the precipitation false-positive can be isolated, quantified, and removed.

Previous versions on the atypically-thick low marine cloud search algorithm were used to tabulate such bias information. Changes in the 3A12 product, corrected by removing raining pixels identified via the search algorithm, are as high as 75% in marine stratocumulus regions. Since rainfall amounts are typically low in those regions, any change in reported rainfall would have large impact. The peak unconditional climatological rain rate difference was 0.05 mm/hr, over the East China Sea where atypically-thick low marine clouds occur most often. The ITCZ, where the majority of oceanic rainfall occurs, did not appear to be significantly biased. Performing bias corrections using the newest iteration of the search algorithm is an item of future work and will benefit other research by providing information to improve global precipitation products.

#### **4.1.2 MODIS Cloud Properties Analysis**

A systematic accounting of the MODIS estimated cloud properties for atypically-thick low marine clouds can be compiled which may provide more information about their structure and behavior. A MODIS sensor is on the same satellite as the AMSR-E sensor. MODIS provides a wide variety of information about cloud properties including: aerosol optical depth, cloud fraction, cloud top pressure, cloud top temperature, effective radius, and cloud water path, and droplet number concentration.

The identification of atypically thick clouds using AMSR-E provides a constraint on cloud thickness. By relating cloud thickness, droplet effective radius, liquid water path,

and droplet number concentration, the distribution and joint variation of these parameters can be examined.

### **4.1.3 Systematic CloudSat Thickness Assessment**

The Aqua satellite and CloudSat are both part of the A-Train satellite constellation. As a result, the sensors aboard both satellites make nearly concurrent observations of the same locations. CloudSat features a vertically profiling cloud resolving radar capable of producing high-resolution information about the vertical structure of clouds. As an avenue for future research, we can use the search algorithm on AMSR-E data to identify atypically thick low marine clouds that also have CloudSat observations. CloudSat is capable of resolving cloud droplet size hydrometeors with a vertical resolution of 500 m. Key limitations of CloudSat are limited sample size and data quality problems in the lowest few gates near the ocean surface, critical for distinguishing cloud from fog. Despite these limitations CloudSat may be able to add additional information about microphysical processes within atypically thick low marine clouds. Contoured frequency by altitude diagrams (CFADs) [Yuter and Houze 1995b] show how the mode of radar reflectivity changes with height in drizzling stratocumulus (Comstock et al. 2007). Using CloudSat derived CFADs to investigate atypically thick low marine clouds will provide information on the vertical variations of the mode of reflectivity and allow for inferences about droplet grow rates and mechanisms. Automation of such a task will be a challenge both from the standpoint of developing software to do the cross-product data analysis and

from the computer resources necessary for concurrently hosting both the AMSR-E and CloudSat data needed for such a study.

#### **4.1.4 Field and Modeling Studies**

Satellite data alone cannot provide a complete picture of the physical characteristics, genesis, and evolution of atypically-thick low marine clouds since current passive microwave satellite data sets do not have sufficient temporal resolution to address the details of cloud evolution.

The greatest leap in understanding of the nature of atypically-thick low marine clouds is likely to come from field studies. Aircraft and/or ship-based observations will be able to provide a great deal of information about the evolution of atypically-thick low marine clouds that can be gathered no other way. Information from Chapter II about the areas where and when atypically-thick low marine clouds occur most frequently provides a good starting place for the planning of a field observation campaign. Field studies, such as EPIC Sc and VOCALS in the case of marine stratocumulus in the Southeast Pacific, have proven very successful at improving our understanding of other cloud and precipitation phenomena, particularly those that occur over the open ocean where systematic surface-based observation are difficult or impossible. New observing platforms, such as the NASA Global Hawk, provide opportunities for detailed sampling in remote areas of the ocean.

The track record of current global forecast and climate models in accurately representing low clouds is poor (Bony and Dufresne 2005, Bony et al. 2006). Modeling of atypically

thick low marine clouds in a Large-Eddy-Simulation framework will likely be more fruitful in the near term than examination of currently available reanalysis or IPCC model output.

## **4.2 Using 89 GHz Drizzle Detection for Climate Study**

Chapter III discussed the potential and feasibility of using passive microwave 89 GHz brightness temperature data to detect areas of drizzle in marine stratocumulus. While that chapter illustrated the potential utility of detecting drizzle using 89 GHz data, there remains much work to turn a data analysis method into improved understanding of marine stratocumulus.

Due in part to their importance to the global climate, three of the five marine stratocumulus regions have been previously studied in extensive field campaigns (Northeast Pacific off the coast of California – FIRE, DYCOMS and DYCOMS II; Southeast Pacific off the coasts of Peru and Chile – PACS, EPIC Sc, and VOCALS; Northeast Atlantic centered on the Azores – ASTEX and currently CAP-MBL). Comparison of aircraft and ship observations made during DYCOMS II, EPIC Sc, and VOCALS indicates that maximum observed drizzle rates are higher in the Southeast Pacific compared to the Northeast Pacific. The regions in the Southeast Atlantic off the coast of Angola and the Southeast Indian Ocean off the coast of Australia have never been directly observed and where these regions fit among the other regions remains a significant missing piece in our understanding of marine stratocumulus. While intense periods of direct observations with ship and aircraft provide the foundation for much of

our current understanding of stratocumulus cloud deck, routine ship and aircraft observations on yearly basis are not feasible. To study features of open-ocean marine stratocumulus on longer time scales or to make comparisons among the five marine stratocumulus regions, we must rely on global satellite remote sensing.

To that end, future work using 89 GHz data to identify drizzle and quantify the spatial frequency and extent of that drizzle will allow for the interannual trends in drizzle to be examined for the stratocumulus regions. Additionally, such analyses will allow for the intercomparison of drizzle characteristics between different stratocumulus regions.

Differences and similarities between the regions will be tabulated and used to determine to what degree the understanding gained from observations obtained in the Pacific are applicable to the less studied Southeast Atlantic.

The ability of passive microwave sensors to glean information on the total column properties of clouds and precipitation provides greater utility than more common visible and infrared-based sensors. Vertically-pointing active sensors such as cloud radar and lidar provide profiles which contain more information than vertically-integrated properties from passive microwave. However, the practical reality is that current cloud-profiling sensors on CloudSat and Calipso are nadir-pointing only and have much smaller sample sizes than the swath-scanning passive microwave sensors. The multitude of passive microwave sensors currently in orbit provide the best opportunity with the current generation of satellites of constructing a global climatology of an intermittent and small-scale cloud phenomena such as marine stratocumulus drizzle.

## REFERENCES

- Ackerman, A. S., O. B. Toon, J. P. Taylor, D. W. Johnson, P. V. Hobbs, and R. J. Ferek (2000), Effects of Aerosols on Cloud Albedo: Evaluation of Twomey's Parameterization of Cloud Susceptibility Using Measurements of Ship Tracks, *J. Atmos. Sci.*, 57(16), 2684-2695.
- Atkinson, B. W. and J. Wu Zhang (1996), Mesoscale Shallow Convection in the Atmosphere, *Rev. Geophys.*, 34(4), 403-431, doi: 10.1029/96RG02623.
- Baker, M. B. (1997), Cloud Microphysics and Climate, *Science*, 276(5315), 1072-1078, doi: 10.1126/science.276.5315.1072.
- Berg, W., T. L'Ecuyer, and C. Kummerow (2006), Rainfall Climate Regimes: The Relationship of Regional TRMM Rainfall Biases to the Environment, *Journal of Applied Meteorology and Climatology*, 45(3), 434-454.
- Bretherton, C. S., T. Uttal, C. W. Fairall, S. Yuter, R. Weller, D. Baumgardner, K. Comstock, and R. Wood (2004), The EPIC 2001 stratocumulus study, *Bull. Amer. Meteor. Soc.*, 85, 967-977.
- Bony, S. and J. Dufresne (2005), Marine boundary layer clouds at the heart of tropical cloud feedback uncertainties in climate models, *Geophys. Res. Lett.*, 32(20), L20806, doi: 10.1029/2005GL023851.

- Bony, S. et al. (2006), How Well Do We Understand and Evaluate Climate Change Feedback Processes?, *J. Clim.*, 19(15), 3445-3482.
- Coakley, J. A. and C. D. Walsh (2002), Limits to the Aerosol Indirect Radiative Effect Derived from Observations of Ship Tracks, *J. Atmos. Sci.*, 59(3), 668-680.
- Comstock, K. K., C. S. Bretherton, and S. E. Yuter (2005) Mesoscale variability and drizzle in southeast Pacific stratocumulus, *J. Atmos. Sci.*, 62, 3792-3807.
- Comstock, K., S. E. Yuter, R. Wood, and C. S. Bretherton (2007), The three-dimensional structure and kinematics of drizzling stratocumulus, *Mon. Wea. Rev.*, 135, 3767-3784.
- Colman, R. (2003), A comparison of climate feedbacks in general circulation models, *Clim. Dyn.*, 20(7), 865-873.
- Crewell, S. and U. Löhnert (2003), Accuracy of cloud liquid water path from ground-based microwave radiometry 2. Sensor accuracy and synergy, *Radio Science*, 38, doi:10.29/2002RS002634.
- Donlon, C. J., P. J. Minnett, C. Gentemann, T. J. Nightingale, I. J. Barton, B. Ward, and M. J. Murray (2002), Toward improved validation of satellite sea surface skin temperature measurements for climate research, *J. Clim.*, 15, 353-3659.
- Frisch, A. S., C. W. Fairall, and J. B. Snider (1995), Measurement of Stratus Cloud and Drizzle Parameters in ASTEX with a K $\alpha$ -Band Doppler Radar and a Microwave Radiometer, *J. Atmos. Sci.*, 52(16), 2788-2799.

- George, R. C. and R. Wood (2010), Subseasonal variability of low cloud radiative properties over the southeast Pacific Ocean, *Atmos. Chem. Phys.*, 10, 4047-4063, doi:10.5194/acp-10-4047-2010.
- Gerber, H., G. Frick, S. P. Malinowski, J. -. Brenguier, and F. Burnet (2005), Holes and Entrainment in Stratocumulus, *J. Atmos. Sci.*, 62(2), 443-459.
- Greenwald, T. J., T. S. L'Ecuyer, and S. A. Christopher (2007), Evaluating specific error characteristics of microwave derived cloud liquid water products, *Geophys. Res. Lett.*, 34, doi:10.1029/2007GL31180.
- Greenwald, T. J. (2009), A 2 year comparison of AMSR-E and MODIS cloud liquid water path observations, *Geophys. Res. Lett.*, 36, doi:10.1029/2009GK040394.
- Grossman, R. L. and A. K. Betts (1990), Air–Sea Interaction during an Extreme Cold Air Outbreak from the Eastern Coast of the United States, *Mon. Weather Rev.*, 118(2), 324-342.
- Haralick, R. M. and L. G. Shapiro (1992), *Computer and Robot Vision*, 630 pp., Addison-Wesley Longman Publishing Co., Inc.
- Harrison, E. F., P. Minnis, B. R. Barkstrom, V. Ramanathan, R. D. Cess, and G. G. Gibson (1990), Seasonal Variation of Cloud Radiative Forcing Derived From the Earth Radiation Budget Experiment, *J. Geophys. Res.*, 95, 18687-18703, doi: 10.1029/JD095iD11p18687.

- Harrold, T. W. (1973), Mechanisms influencing the distribution of precipitation within baroclinic disturbances, *Q. J. R. Meteorol. Soc.*, 99(420), 232-251.
- Hartmann, D. L., M. Ockert-Bell, and M. L. Michelsen (1992), The Effect of Cloud Type on Earth's Energy Balance: Global Analysis, *J. Clim.*, 5(11), 1281-1304.
- Hayasaka, T., T. Nakajima, Y. Fujiyoshi, Y. Ishizaka, T. Takeda, and M. Tanaka (1995), Geometrical Thickness, Liquid Water Content, and Radiative Properties of Stratocumulus Clouds over the Western North Pacific, *J. Appl. Meteorol.*, 34(2), 460-470.
- Haynes, J. and G.L. Stephens (2007), Tropical oceanic cloudiness and the incidence of precipitation: Early results from CloudSat, *Geophys. Res. Lett.*, 34, L09811, doi:10.1029/2007GL029335.
- Hogan, R. J., N. Gaussiat, and A. J. Illingworth (2005), Stratocumulus Liquid Water Content from Dual-Wavelength Radar, *J. Atmos. Ocean. Technol.*, 22(8), 1207-1218.
- Horváth, A., and C. Gentemann (2007), Cloud-fraction-dependent bias in satellite liquid water path retrievals of shallow, non-precipitating marine clouds, *Geophys. Res. Lett.*, 34, doi:10.1029/2007GL030625.
- Im, E., Chialin Wu, and S. L. Durden (2005), Cloud profiling radar for the CloudSat mission, *Radar Conference, 2005 IEEE International*.
- Ishizaka, Y. et al. (2003), The effect of air-pollutants on the microphysical properties of clouds over the sea off the southwest of Kyushu in Japan. *Findings and current problems*

*in the Asian Particle Environmental Change Studies: 2003, JST/CREST/APEX 2003 Interim Report*, 103-116.

Kanamitsu, M., W. Ebisuzaki, J. Woollen, S. Yang, J. J. Hnilo, M. Fiorino, and G. L. Potter (2002), NCEP–DOE AMIP-II Reanalysis (R-2), *Bull. Am. Meteorol. Soc.*, 83(11), 1631-1643.

Karstens, U., C. Simmer, and E. Ruprecht (1994), Remote sensing of cloud liquid water, *Meteorology and Atmospheric Physics*, 54(1), 157-171.

Kawanishi, T., T. Sezai, Y. Ito, K. Imaoka, T. Takeshima, Y. Ishido, A. Shibata, M. Miura, H. Inahata, and R. W. Spencer (2003), The Advanced Microwave Scanning Radiometer for the Earth Observing System (AMSR-E), NASDA's contribution to the EOS for global energy and water cycle studies, *Geoscience and Remote Sensing, IEEE Transactions on*, 41(2), 184-194.

Kida, S., S. Shige, T. Kubota, K. Aonashi, and K. Okamoto (2009), Improvement of Rain/No-Rain Classification Methods for Microwave Radiometer Observations over the Ocean Using a 37 GHz Emission Signature, *Journal of the Meteorological Society of Japan*, 87A, 165-181.

Klein, S. A. and D. L. Hartmann (1993), The Seasonal Cycle of Low Stratiform Clouds, *J. Clim.*, 6(8), 1587-1606.

Koračin, D., J. Lewis, W. T. Thompson, C. E. Dorman, and J. A. Businger (2001), Transition of Stratus into Fog along the California Coast: Observations and Modeling, *J. Atmos. Sci.*, 58(13), 1714-1731.

Kummerow, C., W. S. Olson, and L. Giglio (1996), A simplified scheme for obtaining precipitation and vertical hydrometeor profiles from passive microwave sensors, *Geoscience and Remote Sensing, IEEE Transactions on*, 34(5), 1213-1232.

Kummerow, C., W. Barnes, T. Kozu, J. Shiue, and J. Simpson (1998), The Tropical Rainfall Measuring Mission (TRMM) Sensor Package, *J. Atmos. Ocean. Technol.*, 15(3), 809-817.

Kummerow, C., Y. Hong, W. S. Olson, S. Yang, R. F. Adler, J. McCollum, R. Ferraro, G. Petty, D. Shin, and T. T. Wilheit (2001), The Evolution of the Goddard Profiling Algorithm (GPROF) for Rainfall Estimation from Passive Microwave Sensors, *J. Appl. Meteorol.*, 40(11), 1801-1820.

Liu, Y. and P. H. Daum (2004), Parameterization of the Autoconversion Process. Part I: Analytical Formulation of the Kessler-Type Parameterizations, *J. Atmos. Sci.*, 61(13), 1539-1548.

Liu, Y., P. H. Daum, and R. McGraw (2004), An analytical expression for predicting the critical radius in the autoconversion parameterization, *Geophys. Res. Lett.*, 31, doi: 10.1029/2003GL019117.

- Miller, M. A., J. Verlinde, C. V. Gilbert, G. J. Lehenbauer, J. S. Tongue, and E. E. Clothiaux (1998), Detection of Nonprecipitating Clouds with the WSR-88D: A Theoretical and Experimental Survey of Capabilities and Limitations, *Weather and Forecasting*, 13(4), 1046-1062.
- Negri, A. J., T. L. Bell, and L. Xu (2002), Sampling of the Diurnal Cycle of Precipitation Using TRMM, *J. Atmos. Ocean. Technol.*, 19(9), 1333-1344.
- Noonkester, V. R. (1979), Coastal Marine Fog in Southern California, *Mon. Weather Rev.*, 107(7), 830-851.
- Norris, J. R. (1998), Low Cloud Type over the Ocean from Surface Observations. Part I: Relationship to Surface Meteorology and the Vertical Distribution of Temperature and Moisture, *J. Clim.*, 11(3), 369-382.
- Norris, J. R. (1998), Low Cloud Type over the Ocean from Surface Observations. Part II: Geographical and Seasonal Variations, *J. Clim.*, 11(3), 383-403.
- Norris, J. R. and S. A. Klein (2000), Low Cloud Type over the Ocean from Surface Observations. Part III: Relationship to Vertical Motion and the Regional Surface Synoptic Environment, *J. Clim.*, 13(1), 245-256.
- Oliver, D. A., W. S. Lewellen, and G. G. Williamson (1978), The Interaction between Turbulent and Radiative Transport in the Development of Fog and Low-Level Stratus, *J. Atmos. Sci.*, 35(2), 301-316.

Petty, G. (2006), *A First Course In Atmospheric Radiation*, 457pp., Sundog Publishing, Madison, Wisconsin.

Roberts, G. C., M. V. Ramana, C. Corrigan, D. Kim, and V. Ramanathan (2008), Simultaneous observations of aerosol–cloud–albedo interactions with three stacked unmanned aerial vehicles, *Proceedings of the National Academy of Sciences*, 105(21), 7370-7375, doi: 10.1073/pnas.0710308105.

Rosenfeld, A. and J. L. Pfaltz (1966), Sequential Operations in Digital Picture Processing, *J.ACM*, 13(4), 471-494.

Rossow, W. B. and R. A. Schiffer (1991), ISCCP Cloud Data Products, *Bull. Am. Meteorol. Soc.*, 72(1), 2-20.

Savic-Jovic, V. and B. Stevens (2008), The structure and mesoscale organization of precipitating stratocumulus, *J. Atmos. Sci.*, 65, 1587-1605.

Sharon, T. M., B. A. Albrecht, H. H. Jonsson, P. Minnis, M. M. Khaiyer, T. M. van Reken, J. Seinfeld, and R. Flagan (2006) Aerosol and cloud microphysical characteristics of rifts and gradients in maritime stratocumulus clouds, *J. Atmos. Sci.*, 63, 983–997.

Slingo, J. M. (1980), A cloud parametrization scheme derived from GATE data for use with a numerical model, *Q. J. R. Meteorol. Soc.*, 106(450), 747-770.

Sorooshian, A., G. Feingold, M. D. Lebsock, H. Jiang, and G. L. Stephens (2009), On the precipitation susceptibility of clouds to aerosol perturbations, *Geophys. Res. Lett.*, 36(13), L13803, doi: 10.1029/2009GL038993.

Stephens, G. L. et al. (2002), THE CLOUDSAT MISSION AND THE A-TRAIN, *Bull. Am. Meteorol. Soc.*, 83(12), 1771-1790.

Stephens, G. L., D. G. Vane, S. Taneli, E. Im, S. Durden, M. Rokey, D. Reinke, P. Partain, G. G. Mace, R. Austin, T. L'Ecuyer, J. Haynes, M. Lebsock, K. Sukuki, D. Waliser, D. Wu, J. Key, A. Gettelman, Z. Wang and R. Marchand (2008), Cloudsat mission: Performance and early science after the first year of operation, *J. Geophys. Res.*, 113, doi:10.1029/2008JD009982.

Stevens, B., G. Vali, K. Comstock, R. Wood, M. C. van Zanten, P. H. Austin, C. S. Bretherton, and D. H. Lenschow (2005), Pockets of open cells (POCs) and drizzle in marine stratocumulus, *Bull. Amer. Meteor. Soc.*, 86, 51–57.

Stowe, L. L., C. G. Wellemeyer, H. Y. M. Yeh, T. F. Eck, and The Nimbus-7 CLOUD DATA, PROCessing TEAM (1988), Nimbus-7 Global Cloud Climatology. part I: Algorithms and Validation, *J. Clim.*, 1(5), 445-470.

Twomey, S. (1974), Pollution and the Planetary Albedo, *Atmos. Environ.*, 8, 1251-1256.

Twomey, S. (1977), The Influence of Pollution on the Shortwave Albedo of Clouds, *J. Atmos. Sci.*, 34, 1149-1152.

- van Zanten, M. C., and B. Stevens (2005), On the observed structure of heavily precipitating marine stratocumulus, *J. Atmos. Sci.*, 62, 4327–4342.
- Wang, H. and G. Feingold (2009), Modeling mesoscale cellular structures and drizzle in marine stratocumulus. Part I: Impact of drizzle on the formation and evolution of open cells, *J. Atmos. Sci.*, 66, 3237-3256.
- Wang, J. and W. B. Rossow (1995), Determination of Cloud Vertical Structure from Upper-Air Observations, *J. Appl. Meteorol.*, 34(10), 2243-2258.
- Warren, S. G., C. J. Hahn, J. London, R. M. Chervin, R. L. D. o. A. S. Jenne, Colorado Univ., Boulder, CO. Cooperative Inst. for Research in Environmental Sciences, Colorado Univ., Boulder, CO. Dept. of Astrophysical, Planetary, and Atmospheric Sciences, and National Center for Atmospheric Research, Boulder, CO (1988), *Global distribution of total cloud cover and cloud type amounts over the ocean*, Medium:-ED; Size: Pages: (305 p).
- Webb, M. et al. (2006), On the contribution of local feedback mechanisms to the range of climate sensitivity in two GCM ensembles, *Clim. Dyn.*, 27(1), 17-38.
- Wentz, F. J., and T. Meissner (2000), *AMSR Ocean Algorithm, Version 2*, vol. 121599A-1, p. 66, Remote Sensing Systems, Santa Rosa, CA.
- Wentz, F., and T. Meissner (2004), AMSR-E/Aqua L2B Global Swath Ocean Products Derived from Wentz Algorithm V002, <http://www.nsidc.org/data/modis>, National Snow and Ice Data Center, Boulder, Colorado, USA. (Updated daily.)

Westwater, E. R., Y. Han, M. Shupe, and S. Y. Matrosov (2001), Analysis of integrated cloud liquid and precipitable water vapor retrieval from microwave radiometers during the Surface Heat Budget of the Arctic Ocean project, *J. Geophys. Res.*, 106, 32,019-32,030.

Wood, R., C. S. Bretherton, D. Leon, A. D. Clarke, P. Zuidema, G. Allen, and H. Coe (2010), An aircraft case study of the spatial transition from closed to open mesoscale cellular convection, Submitted *Atmos. Chem. Phys.*.

Wyant, M., C. Bretherton, J. Bacmeister, J. Kiehl, I. Held, M. Zhao, S. Klein, and B. Soden (2006), A comparison of low-latitude cloud properties and their response to climate change in three AGCMs sorted into regimes using mid-tropospheric vertical velocity, *Clim. Dyn.*, 27(2), 261-279.

Wyant, M.C., and Coauthors (2009), The PreVOCA experiment: modeling the lower troposphere in the Southeast Pacific, *Atmos. Chem. Phys.*, 9, 23909-23953.

Yao, M. and A. D. Del Genio (2002), Effects of Cloud Parameterization on the Simulation of Climate Changes in the GISS GCM. Part II: Sea Surface Temperature and Cloud Feedbacks, *J. Clim.*, 15(17), 2491-2503.

Yuter, S. E. and R. A. Houze (1995), Three-Dimensional Kinematic and Microphysical Evolution of Florida Cumulonimbus. Part II: Frequency Distributions of Vertical Velocity, Reflectivity, and Differential Reflectivity, *Mon. Weather Rev.*, 123(7), 1941-1963.

Zhang, M. H. et al. (2005), Comparing clouds and their seasonal variations in 10 atmospheric general circulation models with satellite measurements, *J. Geophys. Res.*, 110, D15S02, doi: 10.1029/2004JD005021.